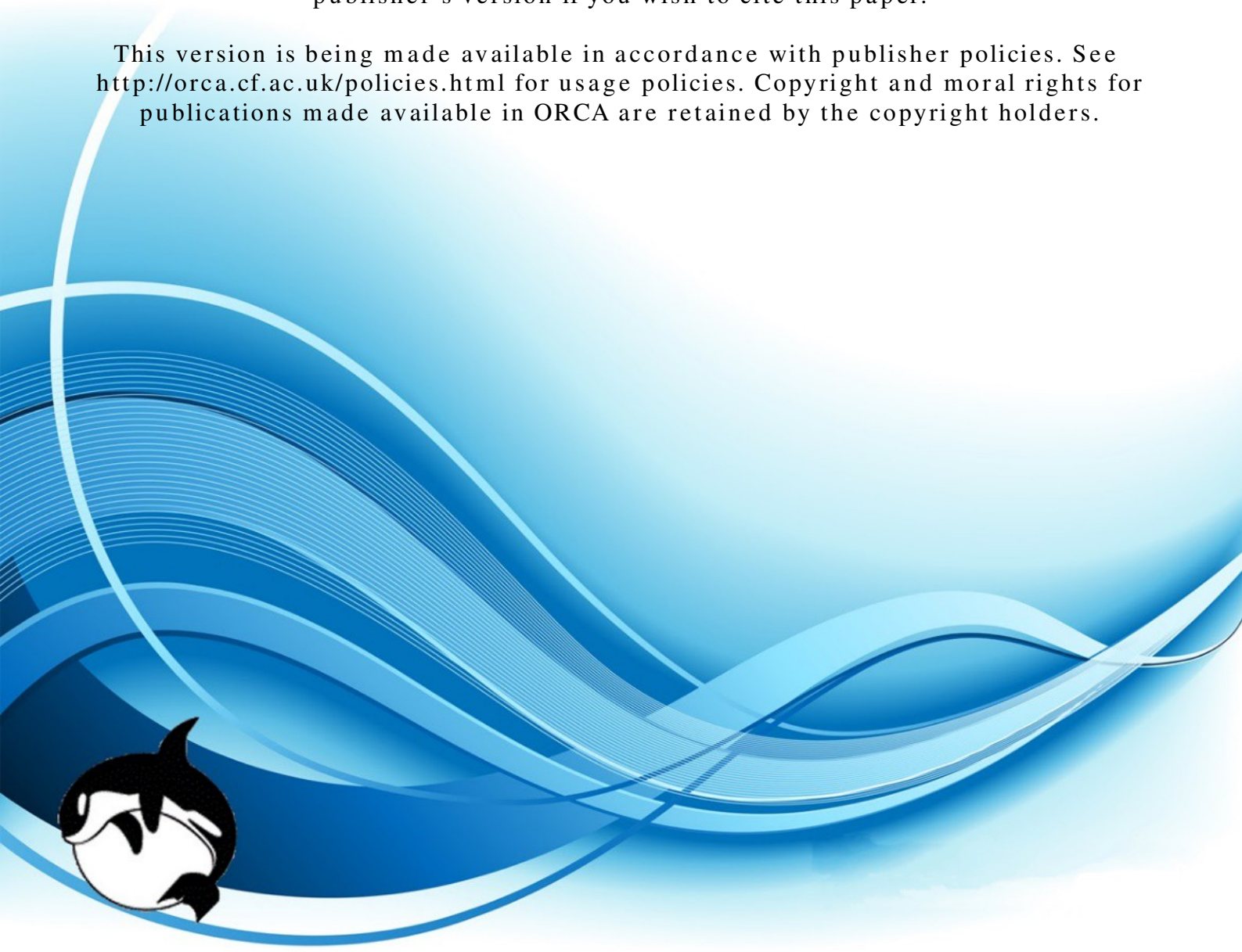

Boundary variation diminished conservative semi-Lagrangian method for both compressible and incompressible flows

Qijie Li (李启杰)[a], Junqiang Xia (夏军强)[a,*], Kensuke Yokoi[b,*], Syazana Omar[b]

[a] *State Key Laboratory of Water Resources and Hydropower Engineering, Wuhan University, Wuhan, 430072, China*
[b] *School of Engineering, Cardiff University, Cardiff, CF24 3AA, United Kingdom*

Abstract

Motivated by the enlightenment that diminishing the jump at the cell boundary can effectively reduce numerical dissipation near the critical region, a novel constrained interpolation profile conservative semi-Lagrangian method is proposed based on a newly designed boundary variation diminishing (BVD) algorithm. Firstly, a constrained interpolation profile conservative semi-Lagrangian scheme with the piecewise tangent of hyperbola for interface capturing scheme (CIP-CSL-THINC) is proposed as one candidate to represent jump-like discontinuities. Secondly, the constrained interpolation profile conservative semi-Lagrangian scheme with a fourth-order weighted essentially non-oscillatory limiter (CIP-CSL-WENO4) is used as another candidate to keep the high-order and non-oscillatory reconstruction for smooth solutions. The selection criterion of these two candidates is designed by minimizing the total variations of the first derivative at cell boundaries. An unified pressure-based projection formulation with a fractional step procedure is implemented with the proposed scheme to simulate both compressible and incompressible flows. A variety of numerical tests are studied, including linear and nonlinear scalar wave transport problems, and compressible and incompressible flows problems. Results show that the proposed method can effectively eliminate numerical oscillation and diffusion, suggesting it has great potential to be applied to various types of engineering problems including both compressible and incompressible flows.

Keywords: BVD, CIP-CSL, WENO, Tangent hyperbolic function, Compressible flow, Incompressible flow

1. Introduction

Numerical simulations of fluid phenomena with both compressible and incompressible flows are widely used in industrial applications [1–4], such as flows in the combustor of an engine [5–7], flows around turbomachinery blades [8, 9], flows past an aerodynamic body at a high attack angle [10, 11], and cavitating flows where a very low Mach number of nearly incompressible flows may coexist with high Mach number supersonic compressible flows [12–15]. In order to solve these complex flow problems robustly, sharp interface methods must be developed to correctly resolve the interaction of compressible and incompressible flows. Toward this goal, efforts have been made to explore Mach uniform methods based on density-based and pressure-based frameworks [16–25]. On the one hand, density-based methods can be extended to low Mach number flows using sophisticated spatial discretization method for flows of wide

*Corresponding author
Email addresses: xiajq@whu.edu.cn (Junqiang Xia (夏军强)), Kensuke.Yokoi@cardiff.ac.uk (Kensuke Yokoi)

Mach numbers [24]. Although density-based methods are capable of low Mach number flows, this approach is usually subjected to the restriction of time step for computational stability. On the other hand, pressure-based methods can be extended to high Mach number flows by considering acoustic terms in the implicit formulation for pressure or pressure correction [16–18, 25]. With this implementation, the restriction on time step can be resolved using the implict or semi-implicit schemes for pressure projection in pressure-based methods. Following this approach, an unified conservative conservative formulation for all Mach number regimes [16, 17] was proposed using multi-integrated moments method, which presents stable and accurate numerical solutions for strong shocks, compressible and incompressible flows. This multi-integrated moments method can trace back to 2001, Yabe et al. [26, 27] proposed an efficient and accurate conservative semi-Lagrangian (CSL) approach coupled with a pressure-based constrained interpolation profiles (CIP) method to compute both compressible and incompressible flows. In CIP-CSL schemes, polynomials are frequently used to reconstruct the interpolation function. The order of reconstruction polynomials in these schemes can vary; the second-order CIP-CSL2 scheme [26] uses a quadratic interpolation function while the third-order CIP-CSL3 [28] scheme uses a cubic interpolation function. In addition to interpolation functions, a piecewise rational function was used in the CIP-CSL-R [29] scheme to preserve the monotone and non-oscillation property for discontinuous solutions. Following the essentially non-oscillatory (ENO) idea [30, 31], Li et.al proposed the CIP-CSL3-ENO [32] scheme by combining two CIP-CSL3 schemes, including the CIP-CSL3D (where D of CSL3D stands for Downwind) scheme and the CIP-CSL3U (U of CSL3U stands for Upwind) scheme. In the CIP-CSL3-ENO scheme, an ENO indicator is designed, which intentionally selects the non-smooth stencil but can efficiently minimize numerical oscillations. Moreover, Sun et.al [33] proposed a weighted essentially non-oscillatory (WENO) limiter for the CIP-CSL scheme (CIP-CSL-WENO4) to achieve fourth-order accuracy for the smooth solution and keep the WENO property [34, 35] for discontinuities. The CIP-CSL-WENO4 scheme manifests the fourth-order accuracy and oscillation-suppressing property for both scalar and Euler conservation laws. However, the numerical diffusion when involving shock waves tends to smear out discontinuities.

Recently, an approach of high-fidelity shock capturing methods are proposed to reduce the numerical dissipation for high-resolution simulation based on a novel concept of boundary variation diminishing (BVD) [18, 36–42]. This conception takes into account the discontinuity being partially represented within the mesh cell by introducing a jump-like reconstruction for developing high-order Godunov schemes. The original BVD method was built by using a high-order polynomial function (e.g. WENO-Z [35]) for the smooth solution and a sigmoid function (e.g. THINC [43, 44]) for the discontinuous solution. With this implementation, numerical dissipation can be effectively reduced in Riemann solver by minimising the variations of the reconstruction values at cell boundaries. Following this idea, several high-resolution methods have been proposed and sucessfully applied in the simulation of compressible flow problems. For instance, an accurate and robust Mach-uniform numerical model on unstructured grids was proposed with BVD treatment by Xie et al. [18]. Low-dissipation methods based on the BVD idea are presented by Deng et al. [37] and Chen et al. [45] using the second-order monotonic upstream-centered scheme for conservation laws (MUSCL), the tangent of hyperbola for interface capturing (THINC) scheme, and the variant of THINC [46] scheme. The proposed methods have been successfully applied for the simulation of stiff detonation waves problems [40],

compressible gas dynamics with reactive fronts [39], and single and multi-phase compressible flows on unstructured grids. Moreover, two-stage BVD algorithms for compressible flows and compressible turbulent flows based on BVD algorithm are designed by Deng et al. [38] and Jiang et al. [47]. The BVD algorithm reduces the reconstructed jumps, which can be expected to effectively improve the numerical solution. For the smooth solution, the BVD reconstruction naturally realize the highest possible interpolation, which tends to find an interface value closer to the continuous true solution. In terms of the discontinuous solution, pursuing higher order polynomials does not necessarily lead to the reduction of the reconstructed boundary jumps. The BVD reconstruction provides a practical and effective guidance to construct high-fidelity schemes for resolving discontinuous solutions.

Although the original BVD reconstruction is design for Godunov-type finite volume method, the superior performance of the BVD reconstruction indicates that there is great potential in developing semi-Lagrangian schemes with better properties based on the BVD principle. Therefore, in this paper, we modified the BVD algorithm and implement it into the CIP-CSL framework based on the CIP-CSL-WENO4 scheme and the newly proposed CIP-CSL-T scheme. To simulate the compressible flow and incompressible flow with a universal treatment, we follow the pressure-based approach and implement the newly proposed conservation solver to a unified pressure-based projection formulation with fractional step procedure [17] for simulating both compressible and incompressible flows. To validate the proposed scheme, several types of benchmark tests have been conducted. Results show that the proposed method can eliminate numerical oscillation and numerical diffusion efficiently.

This paper is organized as follows. In Section 2, the numerical methodology of conventional CIP-CSL schemes, WENO limiter, and the proposed CIP-CSL-T and BVD-CIP-CSL schemes are described. Various numerical tests including linear, non-linear, compressible, and incompressible flow problems in one and two dimensions are presented in Section 3. The paper ends with some conclusions in Section 4.

2. Methodology

To explain the methodology of CIP-CSL schemes and the WENO limiter, a review of CIP-CSL-R [29, 48] scheme and CIP-CSL-WENO4 scheme is given. Then the details of the proposed CIP-CSL-T scheme and BVD-CIP-CSL scheme are demonstrated. For simplicity, we consider the one-dimensional conservation equation as follows

$$\frac{\partial \phi}{\partial t} + \frac{\partial (u\phi)}{\partial x} = 0, \tag{1}$$

where ϕ is the scalar and u is the velocity. The flux function is $f = u\phi$.

2.1. Review of CIP-CSL-R and CIP-CSL-WENO4 schemes

The constrained interpolation profile conservative semi-Lagrangian (CIP-CSL) scheme is a solver for conservation laws based on a multi-moment concept which uses cell average and boundary value as moments. In this section, we give a review of two CIP-CSL schemes including CIP-CSL-R scheme and CIP-CSL-WENO4 scheme.

In CIP-CSL schemes, the i-th cell average value $\bar{\phi}_i$ and cell boundary values $\phi_{i-1/2}$ and $\phi_{i+1/2}$ are defined as the variables. In addition, the interpolated value at the center $\hat{\phi}_i$ is defined as a temporary variable in the following form

$$\hat{\phi}_i = \frac{3}{2}\bar{\phi}_i - \frac{1}{4}(\phi_{i-1/2} + \phi_{i+1/2}). \tag{2}$$

2.1.1. CIP-CSL-R scheme

The CIP-CSL-R [29] scheme is based on the following piecewise rational interpolation function

$$\Phi_i^{CSLR}(x) = \frac{\alpha_i^R \beta_i^R (x - x_{i-1/2})^2 + 2\alpha_i^R (x - x_{i-1/2}) + \phi_{i-1/2}}{\left[1 + \beta_i^R (x - x_{i-1/2})\right]^2}. \tag{3}$$

The interpolation function $\Phi_i^{CSLR}(x)$ is constructed using the following three constraints

$$\begin{cases} \phi_{i-1/2} = \Phi_i^{CSLR}(x_{i-1/2}), \\ \bar{\phi}_i = \frac{\int_{x_{i-1/2}}^{x_{i+1/2}} \Phi_i^{CSLR}(x)dx}{\Delta x}, \\ \phi_{i+1/2} = \Phi_i^{CSLR}(x_{i+1/2}). \end{cases} \tag{4}$$

Using constraints in Eq. (4), the coefficients (α_i^R and β_i^R) can be obtained as follows

$$\alpha_i^R = \beta_i^R \bar{\phi}_i + (\bar{\phi}_i - \phi_{i-1/2})/\Delta x, \tag{5}$$

$$\beta_i^R = \frac{1}{\Delta x}\Big(\frac{|(\phi_{i-1/2} - \bar{\phi}_i)| + \varepsilon}{|(\bar{\phi}_i - \phi_{i+1/2})| + \varepsilon} - 1\Big), \tag{6}$$

where $\varepsilon = 10^{-12}$ is an infinitesimal number to avoid zero division.

2.1.2. CIP-CSL-WENO4 scheme

Recently, a WENO-limiter devised for the CIP-CSL scheme (CIP-CSL-WENO4) was proposed by Sun et al. [33]. The proposed WENO limiter is based on the idea of WENO scheme [34, 35]. This scheme manifests the fourth-order accuracy and oscillation-suppressing property. The methodology of the CIP-CSL-WENO4 scheme is reviewed in this subsection.

The CIP-CSL-WENO4 scheme employs the following third-order polynomial interpolation function

$$\Phi_i^{CSL3}(x) = C_{3,i}^{CSL3}(x - x_{i-1/2})^3 + C_{2,i}^{CSL3}(x - x_{i-1/2})^2 + C_{1,i}^{CSL3}(x - x_{i-1/2}) + C_{0,i}^{CSL3}. \tag{7}$$

These four coefficients ($C_{3,i}^{CSL3}$, $C_{2,i}^{CSL3}$, $C_{1,i}^{CSL3}$, $C_{0,i}^{CSL3}$) are determined by using three constrains($\bar{\phi}_i$, $\phi_{i-1/2}$ and $\phi_{i+1/2}$) in Eq.(4) and a slope at the cell center in the upwind cell ϕ_i'. In CIP-CSL-WENO4 scheme, a fourth-order WENO-limiter is designed to reconstruct the slope ϕ_i'. The computation is built on the three small stencils $S_{\hat{j}} = \{x_{i-1+\hat{j}/2}, x_{i-1/2+\hat{j}/2}, x_{i+\hat{j}/2}\}, \hat{j} = 0, 1, 2$. For each stencil, we can construct a second-degree polynomial $\Phi_i^{\hat{j}}(x)$ with three point values and the first-order derivatives $\phi_i^{'\hat{j}}$ at the cell center. The explicit form of $\phi_i^{'\hat{j}}$ are

$$\phi_i^{'0} = \frac{\phi_{i+1/2} - \phi_{i-1/2}}{\Delta x_i}, \tag{8}$$

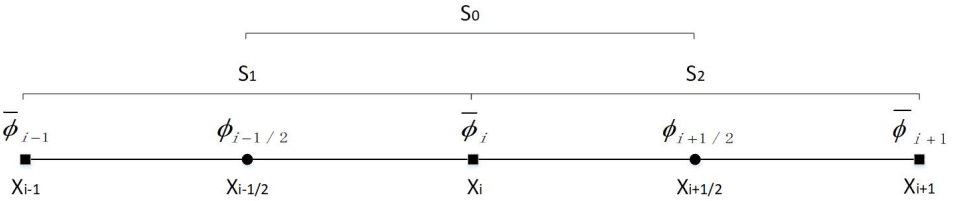

Figure 1: Sketch of the reconstruction stencils for CIP-CSL-WENO4

$$\phi_i'^1 = \frac{3\hat{\phi}_i + \hat{\phi}_{i-1} - 4\phi_{i-1/2}}{\Delta x_i}, \tag{9}$$

$$\phi_i'^2 = -\frac{3\hat{\phi}_i + \hat{\phi}_{i+1} - 4\phi_{i+1/2}}{\Delta x_i}. \tag{10}$$

In CIP-CSL-WENO4 scheme, the first-order derivative ϕ_i' at the cell center with fourth-order accuracy is calculated by using a non-linear combination of $\phi_i'^{\hat{j}}$,

$$\phi_i' = \sum_{\hat{j}=0}^{2} \omega_i^{\hat{j}} \phi_i'^{\hat{j}}. \tag{11}$$

There are several variants proposed to compute the WENO nonlinear weights, such as WENO-JS scheme [34] and WENO-Z scheme [35]. The classical WENO-JS has accuracy loss in the smooth area near the discontinuity. The WENO-Z scheme is able to improve the accuracy of the WENO-JS by using different nonlinear weights and smoothness measurements in the reconstruction. In addition, WENO-Z scheme shows a good balance between numerical accuracy and algorithmic simplicity. Thus, the WENO-Z reconstruction formula is used to calculate the nonlinear weights $\omega_i^{\hat{j}}$ as follows

$$\omega_i^{\hat{j}} = \frac{\alpha_i^{\hat{j}}}{\alpha_i^0 + \alpha_i^1 + \alpha_i^2}, \quad \alpha_i^{\hat{j}} = \gamma_i^{\hat{j}} \Big(1 + \Big(\frac{\tau_0}{\beta_i^{\hat{j}} + \varepsilon}\Big)^P\Big), \tag{12}$$

where the linear parameters are $\gamma_i^0 = \frac{2}{3}$, $\gamma_i^1 = \frac{1}{6}$, and $\gamma_i^2 = \frac{1}{6}$. $\varepsilon = 10^{-12}$ is a small value to prevent division by zero. $\tau_0 = |\beta_i^2 - \beta_i^1|$. The value of P can be selected flexibly to optimise the numerical property of the scheme. $P = 1$ is suggested to control the excessive numerical diffusion in the non-smooth region. In the CIP-CSL-WENO4 scheme, the smoothness indicator is defined as

$$\beta_i^{\hat{j}} = \sum_{l=1}^{2} \int_{x_{i-1/8}}^{x_{i+1/8}} \Delta x^{2l-1} \Big(\frac{\partial^l \Phi_i^{\hat{j}}(x)}{\partial x^l}\Big)^2 dx. \tag{13}$$

The smoothness indicator measures the smoothness of the reconstructed polynomials in the target cell. In the conventional WENO scheme, the upper and lower bound of integration is $x_{i-1/2}$ and $x_{i+1/2}$. In order to match the compact WENO reconstruction stencil of the CIP-CSL scheme, the upper and lower bound of integration in Eq. (13) are adjusted to $x_{i-1/8}$ and $x_{i+1/8}$ respectively.

The explicit form of $\beta_i^{\hat{j}}$ can be expressed as follows

$$\begin{cases} \beta_i^0 = \frac{193}{48}(\phi_{i-1/2} - 2\hat{\phi}_i + \phi_{i+1/2})^2 + \frac{1}{4}(\phi_{i+1/2} - \phi_{i-1/2})^2, \\ \beta_i^1 = \frac{193}{48}(\hat{\phi}_{i-1} - 2\phi_{i-1/2} + \hat{\phi}_i)^2 + \frac{1}{4}(\hat{\phi}_{i-1} - 4\phi_{i-1/2} + 3\hat{\phi}_i)^2, \\ \beta_i^2 = \frac{193}{48}(\hat{\phi}_i - 2\phi_{i+1/2} + \hat{\phi}_{i+1})^2 + \frac{1}{4}(3\hat{\phi}_i - 4\phi_{i+1/2} + \hat{\phi}_{i+1})^2. \end{cases} \tag{14}$$

2.2. The proposed CIP-CSL-T scheme

In this section, we propose a constrained interpolation profile conservative semi-Lagrangian scheme based on the Tangent of Hyperbola for Interface Capturing (THINC) [43, 44, 49, 50] scheme. The proposed reconstruction scheme CIP-CSL-T is devised based on the piecewise tangent hyperbolic function[43] as follows

$$\Phi_i^{CSLT}(x) = \phi_{min} + \frac{\phi_{max} - \phi_{min}}{2}\Big(1 + \gamma^{CSLT}\tanh\Big(\beta^{CSLT}\Big(\frac{x - x_{i-1/2}}{\Delta x} - \tilde{x}_i\Big)\Big)\Big) \tag{15}$$

where $\phi_{min} = \min(\bar{\phi}_{i-1}, \bar{\phi}_{i+1}), \phi_{max} = \max(\bar{\phi}_{i-1}, \bar{\phi}_{i+1})$. $\gamma^{CSLT} = 1$ for $\bar{\phi}_{i-1} < \bar{\phi}_{i+1}$ and $\gamma^{CSLT} = -1$ for $\bar{\phi}_{i-1} > \bar{\phi}_{i+1}$. β^{CSLT} is a prescribed parameter to control the slope and the thickness of the jump. Given β^{CSLT} and γ^{CSLT}, the only unknown parameter left is the jump center $\tilde{x}_i$ is determined by solving

$$\frac{1}{\Delta x}\int_{x_{i-1/2}}^{x_{i+1/2}} \Phi_i^{CSLT}(x)dx = \bar{\phi}_i^n, \tag{16}$$

as

$$\tilde{x}_i = \frac{1}{2\beta^{CSLT}}\ln\Big(\frac{\exp\beta^{CSLT} - A_i}{A_i - \exp(-\beta^{CSLT})}\Big), \tag{17}$$

here

$$A_i = \exp\Big(\frac{\beta^{CSLT}(2C_i - 1)}{\gamma^{CSLT}}\Big) \text{ and } C_i = \frac{\bar{\phi}_i^n - \phi_{min}}{\phi_{max} - \phi_{min}}. \tag{18}$$

To solve Eq. (16), we firstly calculate the fraction of the cell average value $\bar{\phi}_i^n$ base on ϕ_{min} and ϕ_{max} as follows

$$C_i = \frac{\bar{\phi}_i^n - \phi_{min}}{\phi_{max} - \phi_{min}}. \tag{19}$$

C_i can be computed by interpolating the tangent hyperbolic curve as follows

$$C_i = \int_{x_{i-1/2}}^{x_{i+1/2}} \frac{1}{2}\Big(1 + \gamma\tanh\Big(\beta^T\Big(\frac{x - x_{1-1/2}}{\Delta x} - \tilde{x}_i\Big)\Big)\Big), \tag{20}$$

$$C_i = \frac{1}{2\Delta x}\Big[x + \frac{\gamma\Delta x}{\beta^T}\ln\Big(\cosh\Big(\beta^T\Big(\frac{x - x_{1-1/2}}{\Delta x} - \tilde{x}_i\Big)\Big)\Big)\Big]_{x_{i-1/2}}^{x_{i+1/2}}, \tag{21}$$

$$C_i = \frac{1}{2}\Big(1 + \frac{\gamma}{\beta^T}\ln\Big(\frac{\cosh(\beta^T(1 - \tilde{x}_i))}{\cosh(\beta^T\tilde{x}_i)}\Big)\Big), \tag{22}$$

$$C_i = \frac{1}{2}\Big(1 + \frac{\gamma}{\beta^T}\ln(A_i)\Big), \tag{23}$$

with

$$A_i \equiv \frac{\cosh(\beta^T(1 - \tilde{x}_i))}{\cosh(\beta^T\tilde{x}_i)} = \frac{\exp(\beta^T(1 - \tilde{x}_i)) + \exp(-\beta^T(1 - \tilde{x}_i))}{\exp(\beta^T\tilde{x}_i) + \exp(-\beta^T\tilde{x}_i)}. \tag{24}$$

From Eq. (23) we can get

$$\tilde{x}_i = \frac{1}{2\beta^T}\ln\Big(\frac{\exp\beta^T - A_i}{A_i - \exp(-\beta^T)}\Big), \tag{25}$$

where A_i can be computed from Eq. (24)

$$A_i = \exp\frac{\beta^T(2C_i - 1)}{\gamma}. \tag{26}$$

After getting $\tilde{x}_i$, we can get the interpolation function of CIP-CSL-T from Eq. (15).

2.3. The proposed BVD-CIP-CSL scheme

Based on the designed CIP-CSL-T and CIP-CSL-WENO4 schemes, we propose a novel reconstruction scheme by minimizing the total variation of the first-order gradient at cell boundaries for capturing discontinuities. To indicate the smoothness, we calculate the explicit form of β_k[51] for CIP-CSL schemes using $\phi_{i-1/2}, \phi_{i+1/2}$, $\hat{\phi}_{i-1}, \hat{\phi}_i, \hat{\phi}_{i+1}$ as follows

$$\begin{aligned}
\beta_0 &= \frac{52}{3}(\hat{\phi}_{i-1} - 2\phi_{i-1/2} + \hat{\phi}_i)^2 + (\hat{\phi}_{i-1} - 4\phi_{i-1/2} + 3\hat{\phi}_i)^2, \\
\beta_1 &= \frac{52}{3}(\phi_{i-1/2} - 2\hat{\phi}_i + \phi_{i+1/2})^2 + (\phi_{i+1/2} - \phi_{i-1/2})^2, \\
\beta_2 &= \frac{52}{3}(\hat{\phi}_i - 2\phi_{i+1/2} + \hat{\phi}_{i+1})^2 + (3\hat{\phi}_i - 4\phi_{i+1/2} + \hat{\phi}_{i+1})^2.
\end{aligned} \tag{27}$$

Linear combinations of β_k are defined as follows

$$\begin{aligned}
\tau_0 &= |\beta_0 - \beta_2|, \\
\tau_1 &= |\beta_0 - \beta_1|, \\
\tau_2 &= |\beta_1 - \beta_2|.
\end{aligned} \tag{28}$$

Implementing the Taylor series expansions on τ_k and β_k at x_i, we have

$$\begin{aligned}
\beta_0 &= \phi_i'^2\Delta x^2 + (\frac{13}{12}\phi_i''^2 - \frac{1}{6}\phi_i'\phi_i''')\Delta x^4 - \frac{13}{12}\phi_i''\phi_i'''\Delta x^5 + O(\Delta x^6), \\
\beta_1 &= \phi_i'^2\Delta x^2 + (\frac{13}{12}\phi_i''^2 + \frac{1}{12}\phi_i'\phi_i''')\Delta x^4 + O(\Delta x^6), \\
\beta_2 &= \phi_i'^2\Delta x^2 + (\frac{13}{12}\phi_i''^2 - \frac{1}{6}\phi_i'\phi_i''')\Delta x^4 + \frac{13}{12}\phi_i''\phi_i'''\Delta x^5 + O(\Delta x^6),
\end{aligned} \tag{29}$$

$$\begin{aligned}
\tau_0 &= |\frac{13}{6}\phi_i''\phi_i'''\Delta x^5| + O(\Delta x^6), \\
\tau_1 &= |\frac{1}{4}(\phi_i'\phi_i''')\Delta x^4 + \frac{13}{12}\phi_i''\phi_i'''\Delta x^5| + O(\Delta x^6), \\
\tau_2 &= |\frac{1}{4}(\phi_i'\phi_i''')\Delta x^4 - \frac{13}{12}\phi_i''\phi_i'''\Delta x^5| + O(\Delta x^6).
\end{aligned} \tag{30}$$

The above Taylor series expansions suggest that the order of truncation errors of τ_k are much higher than β_k for the smooth solution. Therefore, in smooth region, $\tau_0 = O(\Delta x^5) \ll \beta_k$, $\tau_1 = O(\Delta x^4) \ll \beta_k$, $\tau_2 = O(\Delta x^4) \ll \beta_k$. In this case, $\tau_0 \leq \min(\beta_0, \beta_1, \beta_2)$ or $\tau_1 \leq \min(\beta_0, \beta_1, \beta_2)$ or $\tau_2 \leq \min(\beta_0, \beta_1, \beta_2)$ which suggests the high-order CIP-CSL-WENO4 reconstruction is selected.

In non-smooth region, the reconstruction stencil contains a genuine discontinuity with a certain strength. In this case, the jump-like CIP-CSL-T is prefered to be selected to better represent the discontinuities. As suggested in [43] that diminishing the jump at the cell boundary can effectively reduce numerical dissipation near the cirtical region. In this paper, we apply the BVD algrithm for CIP-CSL-WENO4 and CIP-CSL-T schemes. Firstly, we extend the definition of boundary variation (BV) to the first-order derivative as

$$BV_{x_{i-1/2}} = |\phi'^R_{x_{i-1/2}} - \phi'^L_{x_{i-1/2}}|. \tag{31}$$

Secondly, we define the total boundary variation of the first-order derivatives as

$$TBV = BV_{x_{i-1/2}} + BV_{x_{i+1/2}}. \tag{32}$$

If $TBV^{CSL-T} \leq TBV^{CSL-WENO4}$, which means the total boundary variation of the first-order derivatives can be minimized by selecting the CIP-CSL-T reconstruction. Otherwise, the high-order reconstruction scheme CIP-CSL-WENO4 is used.

In summary, the construction criterion of BVD-CIP-CSL scheme can be expressed as follows

$$\phi_i(x) = \begin{cases} \phi_i^{CSL-WENO4}(x) & \text{if} \quad \tau_0 \leq \min(\beta_0,\beta_1,\beta_2) \quad or \quad \tau_1 \leq \min(\beta_0,\beta_1,\beta_2) \quad or \quad \tau_2 \leq \min(\beta_0,\beta_1,\beta_2), \\ \phi_i^{CSL-T}(x) & \text{else if} \quad TBV^{CSL-T} \leq TBV^{CSL-WENO4}, \\ \phi_i^{CSL-WENO4}(x) & \text{else .} \end{cases} \tag{33}$$

2.4. Time integration method

In terms of the time integration method, the cell average value $\bar{\phi}_i$ and the cell boundary value $\phi_{i-1/2}$ can be updated by a third-order TVD Runge-Kutta formulation [52, 53] based on the CSL formulation. In the third-order TVD Runge-Kutta formulation, we solve the following initial value problem:

$$\frac{\partial X}{\partial t} = -u(X,t). \tag{34}$$

$$X_0 = x_{i-1/2},$$

using the third-order TVD Runge-Kutta method in the following manner

$$X_1 = X_0 - u(X_0,t_0)\Delta t, \tag{35}$$

$$X_2 = \frac{3}{4}X_0 + \frac{1}{4}X_1 - \frac{1}{4}u(X_1,t_1)\Delta t, \tag{36}$$

$$X_3 = \frac{1}{3}X_0 + \frac{2}{3}X_2 - \frac{2}{3}u(X_2,t_2)\Delta t. \tag{37}$$

The temporary cell boundary value $\phi_{i-1/2}^{<k>}$ at each Runge-Kutta time step can be obtained in the following manner

$$\phi_{i-1/2}^{<k>} = \begin{cases} \Phi_{i-1}^{CSL2}(X_k) & \text{if} \quad X_k - X_0 \leq 0 \\ \Phi_i^{CSL2}(X_k) & \text{if} \quad X_k - X_0 > 0, \end{cases} \tag{38}$$

where k is the Runge-Kutta time step. The cell boundary value $\phi_{i-1/2}$ is updated by solving the conservation equation in differential form

$$\frac{\partial \phi}{\partial t} + u\frac{\partial \phi}{\partial x} = -\phi\frac{\partial u}{\partial x}, \tag{39}$$

and the solution is evolved as

$$\phi_{i-1/2}^{n+1} = \phi_{i-1/2}^{<3>} - \frac{\phi_{i-1/2}^{<0>} + \phi_{i-1/2}^{<1>} + 4\phi_{i-1/2}^{<2>}}{6}\frac{\partial u}{\partial x}(X_0)\Delta t. \tag{40}$$

The cell average value $\bar{\phi}_i$ is updated by a finite volume formulation in the following manner

$$\bar{\phi}_i^{n+1} = \bar{\phi}_i^n - \frac{F_{i+1/2} - F_{i-1/2}}{\Delta x}, \tag{41}$$

here

$$F_{i-1/2} = \frac{\phi_{i-1/2}^{<0>} + \phi_{i-1/2}^{<1>} + 4\phi_{i-1/2}^{<2>}}{6} u(X_0). \tag{42}$$

2.5. CIP-CSL schemes for the Euler conservation law

The implementation of CIP-CSL schemes for the one-dimensional Euler conservation laws is described in [53]. Considering 1D Euler equations

$$\mathbf{U}_t + \mathbf{F}(\mathbf{U})_x = 0, \tag{43}$$

where

$$\mathbf{U} = \begin{pmatrix} \rho \\ \rho v \\ E \end{pmatrix}, \quad \mathbf{F}(\mathbf{U}) = \begin{pmatrix} \rho v \\ \rho v^2 + p \\ v(E+p) \end{pmatrix}, \tag{44}$$

the linearised Euler equation about the primitive variables can be obtained as

$$\frac{\partial \mathbf{W}}{\partial t} + \mathbf{A}\frac{\partial \mathbf{W}}{\partial x} = 0, \tag{45}$$

by freezing the Jacobian matrix $\mathbf{A}$, where

$$\mathbf{W} = \begin{pmatrix} \rho \\ v \\ p \end{pmatrix}, \quad \mathbf{A} = \begin{bmatrix} v & \rho & 0 \\ 0 & v & 1/\rho \\ 0 & \rho c^2 & v \end{bmatrix}, \tag{46}$$

here the sound speed $c = \sqrt{\gamma p/\rho}$. Considering the hyperbolicity, the Jacobian matrix $\mathbf{A}$ can be diagonalised by

$$\mathbf{A} = \mathbf{R}\Lambda\mathbf{L}, \tag{47}$$

where Λ is the diagonal matrix of eigenvalues, $\mathbf{L}$ and $\mathbf{R}$ are the matrices of left and right eigenvectors, respectively ($\mathbf{R} = \mathbf{L}^{-1}$). Eq. (45) can be recast into the characteristic form

$$\mathbf{L}\frac{\partial \mathbf{W}}{\partial t} + \Lambda\mathbf{L}\frac{\partial \mathbf{W}}{\partial x} = 0, \tag{48}$$

where

$$\Lambda = \begin{bmatrix} v & 0 & 0 \\ 0 & v+c & 0 \\ 0 & 0 & v-c \end{bmatrix}, \quad \mathbf{L} = \begin{bmatrix} 1 & 0 & -\frac{1}{c^2} \\ 0 & 1 & \frac{1}{\rho c} \\ 0 & 1 & -\frac{1}{\rho c} \end{bmatrix}. \tag{49}$$

For each characteristic direction $\frac{\mathrm{d}x}{\mathrm{d}t} = \lambda_k$, and the characteristic speeds $\lambda_1 = v, \lambda_2 = v + c$ and $\lambda_3 = v - c$ are the non-zero diagonal values of Λ. From Eq. (48), a decoupled system for the characteristic variables can be obtained as

$$\mathrm{d}\rho - \frac{1}{c^2}\mathrm{d}p = 0 \quad \text{along} \quad \mathscr{C}_1 : \frac{\mathrm{d}x}{\mathrm{d}t} = \lambda_1 = v, \;\; x(t=0) = X_0, \tag{50}$$

$$\mathrm{d}v+\frac{1}{\rho c}\mathrm{d}p=0 \quad \text{along} \quad \mathscr{C}_2:\frac{\mathrm{d}x}{\mathrm{d}t}=\lambda_2=v+c,\ \ x(t=0)=X_0, \tag{51}$$

$$\mathrm{d}v-\frac{1}{\rho c}\mathrm{d}p=0 \quad \text{along} \quad \mathscr{C}_3:\frac{\mathrm{d}x}{\mathrm{d}t}=\lambda_3=v-c,\ \ x(t=0)=X_0, \tag{52}$$

where $\mathscr{C}_k,\ k=1,2,3$ represents each characteristic curve. Then, the primitive variables at $t=t^{n+1}$ can be found by the relations below,

$$\rho(X_0)^{n+1}-\rho(X(\mathscr{C}_1))-\frac{1}{c^2}\{p(X_0)^{n+1}-p(X(\mathscr{C}_1))\}=0, \tag{53}$$

$$v(X_0)^{n+1}-v(X(\mathscr{C}_2))+\frac{1}{\rho c}\{p(X_0)^{n+1}-p(X(\mathscr{C}_2)\}=0, \tag{54}$$

$$v(X_0)^{n+1}-v(X(\mathscr{C}_3))-\frac{1}{\rho c}\{p(X_0)^{n+1}-p(X(\mathscr{C}_3)\}=0, \tag{55}$$

where $X(\mathscr{C}_k), k=1,2,3$ indicates the point solutions on each characteristic curve.

The departure point of cell boundary $x=x_{i-1/2}$ is computed by solving the following trajectory equations along the characteristic curves

$$\begin{cases}\dfrac{\mathrm{d}X}{\mathrm{d}t}=-\lambda_k(X,t),\\ X(t=0)=X_0=x_{i+\frac{1}{2}},\end{cases} \qquad k=1,2,3. \tag{56}$$

We solve Eq. (56) by using the third-order TVD Runge-Kutta method, which reads

$$\begin{cases}X_1(\mathscr{C}_k)=X_0-\lambda_k(X_0,t_0)\Delta t,\\ X_2(\mathscr{C}_k)=\dfrac{3}{4}X_0+\dfrac{1}{4}X_1(\mathscr{C}_k)-\dfrac{1}{4}\lambda_k(X_0,t_1)\Delta t,\\ X_3(\mathscr{C}_k)=\dfrac{1}{3}X_0+\dfrac{2}{3}X_2(\mathscr{C}_k)-\dfrac{2}{3}\lambda_k(X_0,t_2)\Delta t,\end{cases} \tag{57}$$

Consequently, by solving the linear system Eq. (53), Eq. (54), and Eq. (55) for primitive variables along characteristic curves, we have

$$\begin{aligned}
p_{i+\frac{1}{2}}^{\langle l\rangle}&=\frac{1}{2}\left(p(X_l(\mathscr{C}_2))+p(X_l(\mathscr{C}_3))+\rho_{i+\frac{1}{2}}^{\langle l-1\rangle}c_{i+\frac{1}{2}}^{\langle l-1\rangle}\left(v(X_l(\mathscr{C}_2))-v(X_l(\mathscr{C}_3))\right)\right),\\
v_{i+\frac{1}{2}}^{\langle l\rangle}&=\frac{1}{2}\left(v(X_l(\mathscr{C}_2))+v(X_l(\mathscr{C}_3))+\frac{1}{\rho_{i+\frac{1}{2}}^{\langle l-1\rangle}c_{i+\frac{1}{2}}^{\langle l-1\rangle}}\left(p(X_l(\mathscr{C}_2))-p(X_l(\mathscr{C}_3))\right)\right),\\
\rho_{i+\frac{1}{2}}^{\langle l\rangle}&=\rho(X_l(\mathscr{C}_1))+\frac{1}{(c_{i+\frac{1}{2}}^{\langle l-1\rangle})^2}\left(p_{i+\frac{1}{2}}^{\langle l\rangle}-p(X_l(\mathscr{C}_3))\right),
\end{aligned} \tag{58}$$

where $\rho(x), v(x)$, and $p(x)$ represent the interpolation functions for the primitive variables ρ, v, and p, respectively. Thus $\rho(X_l(\mathscr{C}_k)), v(X_l(\mathscr{C}_k))$, and $p(X_l(\mathscr{C}_k))$ denote the semi-Lagrangian solutions of the primitive variables along characteristic curve $\mathscr{C}_k$ at the l-th Runge-Kutta substep ($l=1,2,3$).

Subsequently, the primitive variables at cell boundary $x = x_{i-\frac{1}{2}}$ of step n+1 can be updated directly by

$$\begin{aligned} p_{i-\frac{1}{2}}^{n+1} &= p_{i-\frac{1}{2}}^{\langle 3 \rangle}, \\ v_{i-\frac{1}{2}}^{n+1} &= v_{i-\frac{1}{2}}^{\langle 3 \rangle}, \\ \rho_{i-\frac{1}{2}}^{n+1} &= \rho_{i-\frac{1}{2}}^{\langle 3 \rangle}. \end{aligned} \tag{59}$$

Analogous to the case of the scalar conservation law, the cell average value of the conservative variables $\overline{\phi}$ are simply updated using a finite volume formulation as

$$\overline{\phi}_i^{n+1} = \overline{\phi}_i^n - \frac{\Delta t}{\Delta x}(\mathbf{F}_{i+\frac{1}{2}} - \mathbf{F}_{i-\frac{1}{2}}), \tag{60}$$

where the numerical flux $\mathbf{F}_{i+\frac{1}{2}}$ can be computed by the numerical integration of the boundary values of the primitive variables at the substeps of the Runge-Kutta integration scheme, i.e.

$$\mathbf{F}_{i+\frac{1}{2}} = \frac{\mathbf{F}(\mathbf{W}_{i+\frac{1}{2}}^{\langle 0 \rangle}) + \mathbf{F}(\mathbf{W}_{i+\frac{1}{2}}^{\langle 1 \rangle}) + 4\mathbf{F}(\mathbf{W}_{i+\frac{1}{2}}^{\langle 2 \rangle})}{6}. \tag{61}$$

2.6. Pressure based fractional step procedure

We extend the proposed algorithm for simulating both compressible and incompressible flows by implementing the unified pressure based projection formulation with fractional step procedure [17]. Considering the following two-dimensional conservation governing equations:

$$\frac{\partial \rho}{\partial t} + \nabla \cdot \mathbf{m} = 0, \tag{62}$$

$$\frac{\partial \mathbf{m}}{\partial t} + \nabla \cdot (\mathbf{m} \otimes \mathbf{u}) = \nabla \cdot \tau - \nabla p, \tag{63}$$

$$\frac{\partial e}{\partial t} + \nabla \cdot (\mathbf{u} e) = \nabla \cdot (\tau \otimes \mathbf{u}) - \nabla \cdot (p\mathbf{u}), \tag{64}$$

where ρ is the density, $\mathbf{u} = (u, v)$ is the velocity, $\mathbf{m} = (\rho u, \rho v)$ is the momentum and e is the total energy density. The pressure p can be obtained by the equation of state $p = (E - \rho u^2/2)(\gamma - 1)$ for the perfect gas. In this paper, the ratio of the specific heats γ is 1.4. For a Newtonian fluid, the viscous shear stress tensor τ can be evaluated as

$$\tau_{\alpha\beta} = \mu \left[\left(\frac{\partial u_\alpha}{\partial \beta} + \frac{\partial u_\beta}{\partial \alpha} - \frac{2}{3}(\nabla \cdot u)\hat{\delta}_{\alpha\beta} \right) \right] \quad \text{with} \quad \alpha, \beta = x, y, \tag{65}$$

where μ is the coefficient of dynamic viscosity and $\hat{\delta}_{\alpha\beta}$ is the Kronecker delta. The above governing equation can be written as

$$\frac{\partial U}{\partial t} + \frac{\partial F(U)}{\partial x} = 0, \qquad U = \begin{bmatrix} \rho \\ \rho u \\ e \end{bmatrix} \qquad F(U) = \begin{bmatrix} \rho u \\ \rho u^2 - \tau + p \\ u(e - \tau + p) \end{bmatrix} \tag{66}$$

The flux $F(U)$ can be divided into an advection part and two non-advection parts as

$$F(U) = F_I(U) + F_{II}(U) + F_{III}(U) = \begin{bmatrix} m \\ mu \\ eu \end{bmatrix} + \begin{bmatrix} 0 \\ -\tau \\ -\tau u \end{bmatrix} + \begin{bmatrix} 0 \\ p \\ pu \end{bmatrix} \tag{67}$$

To solve the above equation, we implement a fractional step apporach as following procedure.

- Step 1: Solving advection part $F_I(U)$.

  To calculte the advection part, the new proposed schemes are used to solve the conservation equation

  $$\frac{\partial}{\partial t}\int_\Omega \phi dV + \int_\Gamma \phi(\mathbf{u}\cdot\mathbf{n})dS = 0 \tag{68}$$

  Using a dimensional spliting formulation [54] on a uniform grid, the procedure can be read as

  In x direction:

  1. Calculte the temporary moments as

  $\phi_{i-1/2,j-1/2} = (\phi_{i,j-1/2} + \phi_{i-1,j-1/2})/2$, $\quad u_{i-1/2,j-1/2} = (u_{i,j-1/2} + u_{i-1,j-1/2})/2$

  2. Update all the moments ($\phi_{i,j}, \phi_{i-1/2,j}, \phi_{i+1/2,j}, \phi_{i,j-1/2}$ and $\phi_{i,j+1/2}$) using the 1D CIP-CSL solver.

  In y direction:

  1. Calculte the temporary moments as

  $\phi_{i-1/2,j-1/2} = (\phi_{i-1/2,j} + \phi_{i-1/2,j-1})/2$, $\quad u_{i-1/2,j-1/2} = (u_{i-1/2,j} + u_{i-1/2,j-1})/2$

  2. Update all the moments ($\phi_{i,j}, \phi_{i,j-1/2}, \phi_{i,j+1/2}, \phi_{i-1/2,j}$ and $\phi_{i+1/2,j}$) using the 1D CIP-CSL solver.

  Given all the physical variables from step n. After this stage, density ρ is updated to the value at $(n+1)$ th step, while momentum $\mathbf{m}$ and energy e are temporary values and needed to be further advanced by calculating the non-advection parts.

- Step 2: Solving non-advection part $F_{II}(U)$.

  Non-advection part $F_{II}(U)$ is related to viscosity term, which can be computed by a standard finite volume formulation for the value of cell average moments as

  $$\frac{1}{\rho}\int_\Gamma \tau\cdot\mathbf{n}dS = \frac{1}{\rho_{i,j}}\left(\frac{\tau_{i+1/2,j}-\tau_{i-1/2,j}}{\Delta x} + \frac{\tau_{i,j+1/2}-\tau_{i,j-1/2}}{\Delta y} \right). \tag{69}$$

  The value of cell boundary moments can be updated by the time evolution converting (TEC) [17] formula. At this stage, momentum $\mathbf{m}$ and energy e are still temporary values and needed to be updated by solving the rest non-advection part.

- Step 3: Solving non-advection part $F_{III}(U)$.

In this step, the pressure $p_{i,j}$ at cell center can be obtained by solving the following Poisson equation

$$\nabla^2 p^{n+1} = \frac{1}{\Delta t}\left(-\mathbf{u}\cdot\nabla\rho^{n+1} + \frac{1}{C^2}\frac{p^{n+1}-p}{\Delta t} + \nabla\cdot\mathbf{m} \right) \tag{70}$$

where the sound speed $C = \sqrt{\gamma p/\rho}$. The above equation includes the spatial variations in velocity, and it connects directly to the volume change rate for compressible flow. When the sound speed C becomes infinite or the Mach number $M = u/C$ apporaches zero, the above equation becomes exactly the pressure Poisson equation for incompressible flow [17]. In this paper, we use a preconditioned conjugate gradient method to get the solution of $p_{i,j}$ by solving the above Poisson equation. Subsquently, the value of momentum $\mathbf{m}$ and energy e at $n+1$ time step can be updated by the TEC formula.

The proposed scheme can be parallelized by using Message Passing Interface (MPI) [55] technique. With this technique, domain decomposition was used to split the computation domain into the required number of local subdomains for parallel computing. The message passing interface can be employed for data communication among processors and the local data is assigned for different processors, which leads to better computational load balancing and computational efficiency. This algorithm can also be extended to unstructured grids and the implementation will be a bit more complicated. For readers who would be interested in unstructured grids implementation, it is suggested that using the conception of this algorithm combined with a multi-moment finite volume method, which has been successfully applied to unstructured grids [56–60].

3. Numerical results

In this section, benchmark tests of linear and non-linear advection equations, compressible and incompressible flow problems are tested to verify the proposed schemes. Numerical results are compared with those of the representative CIP-CSL-R, CIP-CSL-WENO4, WENOZ and BVD-WENOZ-THINC schemes.

3.1. Order of accuracy

Conservation equation Eq.(1) is solved with the initial condition $\phi(x,0) = \sin(2\pi x)$ to calculate numerical errors and orders of sine wave propagation. The computation domain is $[0,1]$, $u(x) = 1$ and periodic boundary conditions are used. Five different grid sizes (N = 20, 40, 80, 160 and 320) are used. Errors are defined as follows

$$L_1 = \frac{1}{N}\sum_{i=1}^{N} |\phi_i - \phi_{exact,i}|, \tag{71}$$

$$L_\infty = \max(|\phi_i - \phi_{exact,i}|). \tag{72}$$

Table 1: L_1 and L_∞ errors in sine wave propagation at t=1.

Method	N	L_1 error	L_1 order	L_∞ error	L_∞ order
WENO-Z	20	2.14×10^{-4}	-	3.65×10^{-4}	-
	40	6.40×10^{-6}	5.07	1.03×10^{-5}	5.10
	80	2.00×10^{-7}	5.00	3.18×10^{-7}	5.02
	160	6.32×10^{-9}	4.99	9.96×10^{-9}	5.00
	320	2.04×10^{-10}	4.00	3.20×10^{-10}	4.96
CIP-CSL-R	20	9.73×10^{-3}	-	2.65×10^{-2}	-
	40	2.14×10^{-3}	2.19	1.12×10^{-2}	1.24
	80	5.22×10^{-4}	2.04	4.53×10^{-3}	1.31
	160	1.23×10^{-4}	2.09	1.76×10^{-3}	1.36
	320	2.64×10^{-5}	2.22	6.69×10^{-4}	1.40
CIP-CSL-WENO4	20	4.39×10^{-6}	-	6.65×10^{-6}	-
	40	2.74×10^{-7}	4.00	4.29×10^{-7}	3.95
	80	1.72×10^{-8}	4.00	2.69×10^{-8}	3.99
	160	1.07×10^{-9}	4.00	1.69×10^{-9}	4.00
	320	6.73×10^{-11}	4.00	1.06×10^{-10}	4.00
CIP-CSL-T	20	1.78×10^{-1}	-	3.59×10^{-1}	-
	40	7.49×10^{-2}	1.25	2.11×10^{-1}	0.77
	80	3.78×10^{-2}	0.99	1.17×10^{-1}	0.85
	160	1.80×10^{-2}	1.07	6.18×10^{-2}	0.92
	320	1.02×10^{-2}	0.82	3.81×10^{-2}	0.70
BVD-WENOZ-THINC	20	2.14×10^{-4}	-	3.65×10^{-4}	-
	40	6.40×10^{-6}	5.07	1.03×10^{-5}	5.10
	80	2.00×10^{-7}	5.00	3.18×10^{-7}	5.02
	160	6.32×10^{-9}	4.99	9.96×10^{-9}	5.00
	320	2.04×10^{-10}	4.00	3.20×10^{-10}	4.96
BVD-CIP-CSL	20	4.39×10^{-6}	-	6.65×10^{-6}	-
	40	2.74×10^{-7}	4.00	4.29×10^{-7}	3.95
	80	1.72×10^{-8}	4.00	2.69×10^{-8}	3.99
	160	1.07×10^{-9}	4.00	1.69×10^{-9}	4.00
	320	6.73×10^{-11}	4.00	1.06×10^{-10}	4.00

Table 1 shows the numerical results of WENO-Z, CIP-CSL-R, CIP-CSL-WENO4, CIP-CSL-T, BVD-WENOZ-THINC, and BVD-CIP-CSL. It is found that CIP-CSL-T has the lowest accuracy for smooth solutions because of

its jump-like property. However, both BVD-CIP-CSL and CIP-CSL-WENO4 have the highest accuracy and achieve 4th-order accuracy for L_1 and L_∞. This indicates that the implementation of BVD algorithm can select the highest reconstruction candidate in smooth region automatically. This is consistent with the observation of WENO-Z and BVD-WENOZ-THINC schemes.

3.2. Analysis of the computation efficiency

In this section, we measure the computational efficiency of the proposed BVD-CIP-CSL scheme by calculating the computational cost of the advection of a complex wave after one period and making a comparison with WENOZ [35], CIP-CSL-R[29], CIP-CSL-WENO4 [33], and BVD-WENOZ-THINC [36] schemes. The initial conditions are given as

$$\phi(x,0) = \begin{cases} \frac{1}{6}(G(x,\beta,z-\delta)+G(x,\beta,z+\delta)+4G(x,\beta,z)) & \text{if} \quad -0.8 \le x < -0.6 \\ 1 & \text{if} \quad -0.4 \le x < -0.2 \\ 1-|10(x-0.1)| & \text{if} \quad 0.0 \le x < 0.2 \\ \frac{1}{6}(F(x,\alpha,a-\delta)+F(x,\alpha,a+\delta)+4F(x,\alpha,a)) & \text{if} \quad 0.4 \le x < 0.6 \\ 0 & \text{otherwise,} \end{cases} \tag{73}$$

where

$$G(x,\beta,z) = e^{-\beta(x-z)^2}, \tag{74}$$

$$F(x,\alpha,a) = \sqrt{\max(1-\alpha^2(x-a)^2,0)}, \tag{75}$$

here $a = 0.5$, $z = -0.7$, $\delta = 0.005$, $\alpha = 10$ and $\beta = \log(2)/(36\delta^2)$.

In this quantitative measurement, Table 2 presents the mesh number and the CPU time for different schemes to obtain a given level of accuracy (L_1 error = 1.0×10^{-3}). It is found that the proposed BVD-CIP-CSL sheme uses the least mesh number to achieve the given level of accuracy compare to WENOZ, CIP-CSL-R, CIP-CSL-WENO4, and BVD-WENOZ-THINC schemes. In addition, the proposed BVD-CIP-CSL scheme takes the least amount of CPU time compare to other schemes.

Table 2: Computational efficiency for solving complex wave propagation problem. t=2 (1-period) and CFL=0.4

Method	L_1 error	Mesh number	CPU time (s)
WENO-Z	1.0×10^{-3}	5610	43.96
CIP-CSL-R	1.0×10^{-3}	6310	117.71
CIP-CSL-WENO4	1.0×10^{-3}	2300	45.13
BVD-WENOZ-THINC	1.0×10^{-3}	3540	36.24
BVD-CIP-CSL	1.0×10^{-3}	1810	28.47

3.3. Advection equation

To validate the proposed schemes, several types of numerical errors are calculated for a variety of numerical benchmark tests. The total error [61] is defined as

$$E_{Total} = \frac{1}{N}\sum_{i=1}^{N}(\phi_i - \phi_i^e)^2, \tag{76}$$

where ϕ_i^e is the exact solution and ϕ_i is the integrated average numerical solution of the cell i, N is the mesh number. The total error includes two parts: dissipation error represents the gain error (imaginary part in Fourier analysis) and dispersion error represents the phase error (real part in Fourier analysis). It can be defined as

$$E_{Total} = E_{Dissipation} + E_{Dispersion}. \tag{77}$$

The dissipation error and the dispersion error can be calculated by

$$E_{Dissipation} = \left(\sigma(\phi_i) - \sigma(\phi_i^e)\right)^2 + (\bar{\phi}_i - \bar{\phi}_i^e)^2, \tag{78}$$

$$E_{Dispersion} = 2(1-\rho)\sigma(\bar{\phi}_i)\sigma(\phi_i^e), \tag{79}$$

where $\sigma(\phi_i)$ is the standard deviation of numerical solution ϕ_i, and $\sigma(\phi_i^e)$ is the standard deviation of analytical solution ϕ_i^e. $\bar{\phi}_i$, $\bar{\phi}_i^e$ are the mean values of ϕ_i and ϕ_i^e. ρ is the correlation coefficient of ϕ_i and ϕ_i^e, and it is defined as

$$\rho = \frac{\mathrm{cov}(\phi_i, \phi_i^e)}{\sigma(\phi_i)\sigma(\phi_i^e)}, \tag{80}$$

where $\mathrm{cov}(\phi_i, \phi_i^e)$ is the covariance of ϕ_i and ϕ_i^e.

3.3.1. Square wave propagation test

The square wave propagation test is an example of capturing discontinuity. The numerical mesh size is $N = 200$, $\Delta x = 2/N$, $\Delta t = 0.4\Delta x$, $u(x) = 1$, the computational domain is $[-1, 1]$, time is $t = 2$(1-period) and periodic boundary conditions are used in this test. The initial condition is given as

$$\phi(x,0) = \begin{cases} 1 & \text{if} \quad -0.3 \le x < 0.3, \\ 0 & \text{otherwise.} \end{cases} \tag{81}$$

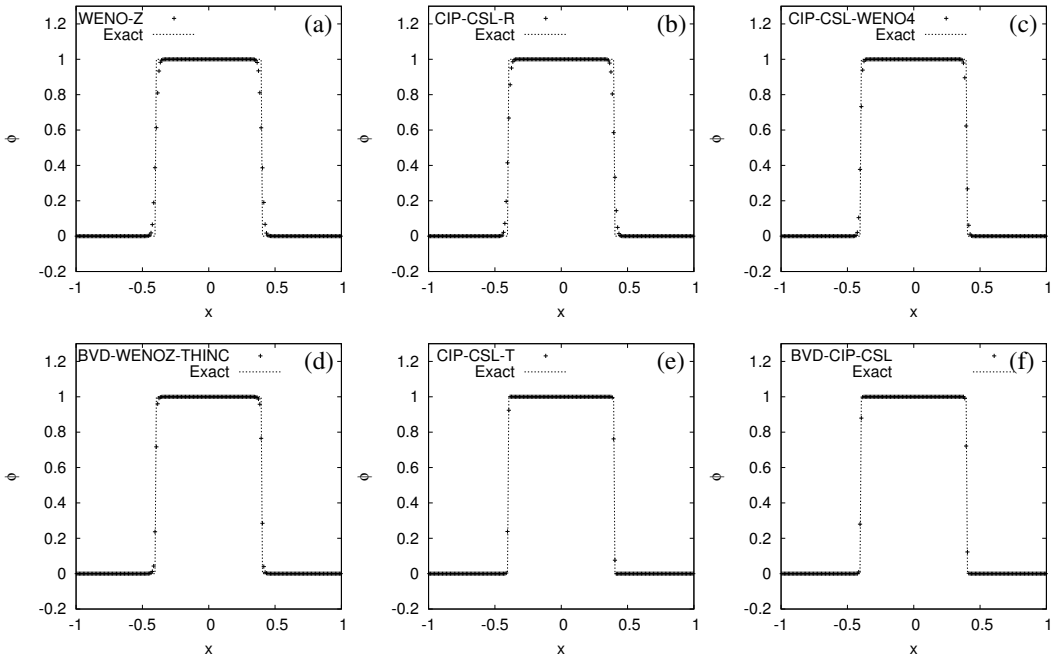

Figure 2: Numerical results of square wave propagation test at t=2. N=200 and CFL=0.4 are used. (a) WENO-Z, (b) CIP-CSL-R, (c) CIP-CSL-WENO4, (d) BVD-WENOZ-THINC, (e) CIP-CSL-T, (f) BVD-CIP-CSL

Table 3: Numerical errors in the square wave propagation test at t=2 (1 periods). N=200 and CFL=0.4 are used.

	Total error	Dissipation error	Dispersion error	L_1 error	L_∞ error
WENO-Z	3.81×10^{-3}	9.72×10^{-5}	3.71×10^{-3}	1.34×10^{-2}	3.87×10^{-1}
CIP-CSL-R	2.40×10^{-3}	6.26×10^{-5}	2.33×10^{-3}	1.09×10^{-2}	3.32×10^{-1}
CIP-CSL-WENO4	1.14×10^{-3}	2.12×10^{-5}	1.12×10^{-3}	6.30×10^{-3}	2.54×10^{-1}
BVD-WENOZ-THINC	1.40×10^{-3}	2.55×10^{-5}	1.37×10^{-3}	6.33×10^{-3}	2.85×10^{-1}
CIP-CSL-T	1.33×10^{-4}	1.70×10^{-6}	1.32×10^{-4}	1.68×10^{-3}	8.27×10^{-2}
BVD-CIP-CSL	2.75×10^{-4}	3.40×10^{-6}	2.72×10^{-4}	2.45×10^{-3}	1.23×10^{-1}

As we can see from Fig. 2, compared with WENO-Z, CIP-CSL-R and CIP-CSL-WENO4 schemes, with the implementation of boundary variation diminishing (BVD) algorithm, numerical dissipation in the vicinity of the discontinuities is reduced effectively. Table 3 shows the total error, numerical dissipation error, numerical dispersion error, L_1 error and L_∞ error of different schemes. Results show that the proposed CIP-CSL-T scheme captures discontinuities sharply with least numerical errors whilst keeping the non-oscillation property. This indicates that using CIP-CSL-T can represent jump-like discontinuities sharply.

3.3.2. complex wave propagation problem

In this case, we test the proposed scheme through Jiang-Shu complex wave propagation problem [34]. The numerical mesh size is $N = 200$, $\Delta x = 2/N$, $\Delta t = 0.4\Delta x$, $u(x) = 1$, the computational domain is $[-1, 1]$ and periodic boundary conditions are used in this test. The initial conditions are the same as those in Sec. 3.2. t=2 and CFL=0.4.

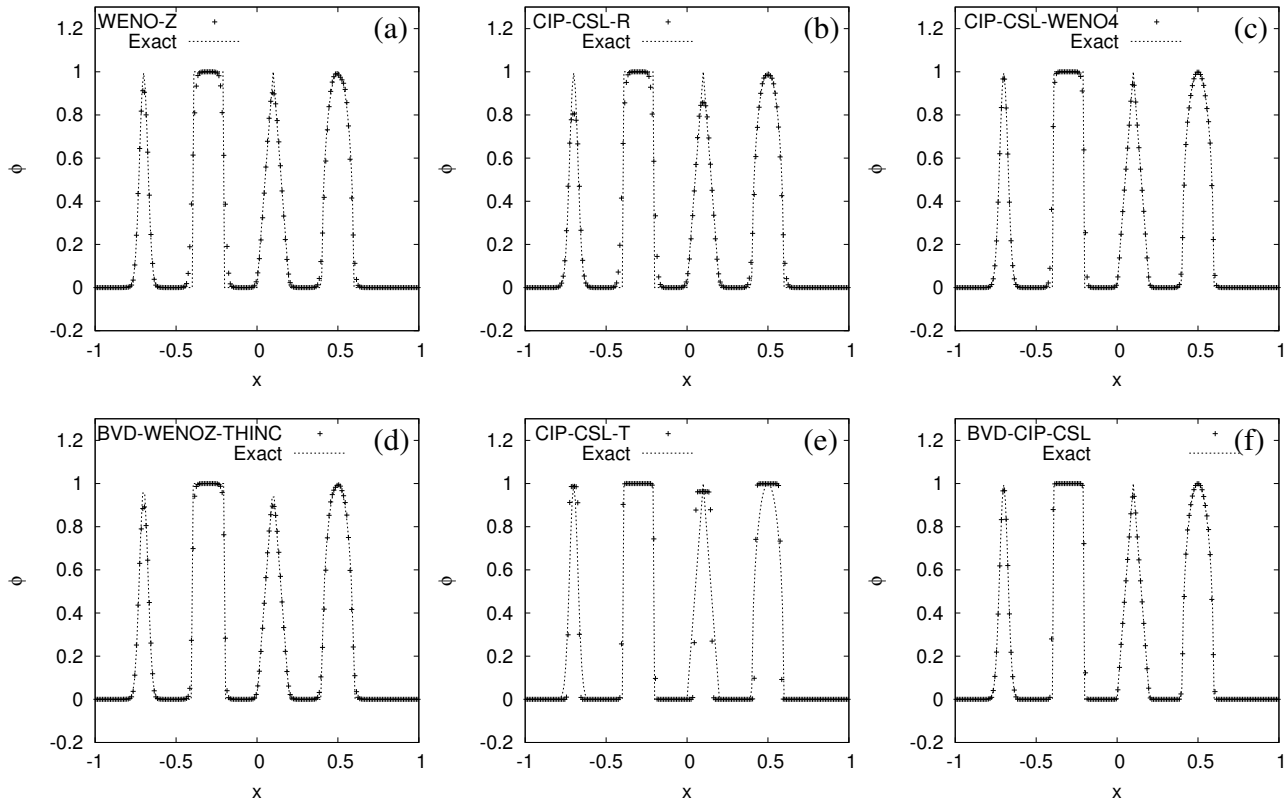

Figure 3: Numerical results of complex wave propagation test at time t=2 (1 period). N=200 and CFL=0.4 are used. (a) WENO-Z, (b) CIP-CSL-R, (c) CIP-CSL-WENO4, (d) BVD-WENOZ-THINC, (e) CIP-CSL-T, (f) BVD-CIP-CSL.

Table 4: Numerical errors in the complex wave propagation test at t=2 (1 periods). N=200 and CFL=0.4 are used.

	Total error	Dissipation error	Dispersion error	L_1 error	L_∞ error
WENO-Z	4.28×10^{-3}	2.47×10^{-4}	4.03×10^{-3}	2.23×10^{-2}	3.87×10^{-1}
CIP-CSL-R	3.23×10^{-3}	2.51×10^{-4}	2.97×10^{-3}	2.24×10^{-2}	3.32×10^{-1}
CIP-CSL-WENO4	1.21×10^{-3}	4.13×10^{-5}	1.17×10^{-3}	8.77×10^{-3}	2.54×10^{-1}
BVD-WENOZ-THINC	2.05×10^{-3}	1.01×10^{-4}	1.95×10^{-3}	1.59×10^{-2}	3.01×10^{-1}
CIP-CSL-T	1.09×10^{-2}	1.11×10^{-3}	9.83×10^{-3}	4.55×10^{-2}	4.43×10^{-1}
BVD-CIP-CSL	3.57×10^{-4}	2.68×10^{-6}	3.54×10^{-4}	5.26×10^{-3}	1.23×10^{-1}

Fig. 3 shows the results at time t=2 (1 periods). It is observed that BVD-CIP-CSL scheme performs better than WENO-Z, CIP-CSL-R, CIP-CSL-WENO4, CIP-CSL-T, and BVD-WENOZ-THINC schemes. Meanwhile, BVD-CIP-CSL scheme has least numerical errors compared to other schemes. This is because that using BVD selection criterion, BVD-CIP-CSL scheme can keep high-order reconstruction for the smooth region and reduce numerical dissipation in the vicinity of the discontinuous region. In the proposed BVD-CIP-CSL scheme, CIP-CSL-WENO4 and CIP-CSL-T are used for smooth and non-smooth regions, respectively.

3.3.3. Extrema of various smoothness problem

In this case, we verify the proposed scheme by capturing extrema of various smoothness test, The numerical mesh size is $N = 100$, the computational domain is $-1 \leq x \leq 1$, $u(x) = 1$ and periodic boundary conditions are used. The initial conditions are given as

$$\phi(x+0.5,0) = \begin{cases} -x\sin(1.5\pi x^2) & \text{if} \quad -1 \leq x < -1/3 \\ |\sin(2\pi x)| & \text{if} \quad |x| \leq 1/3 \\ 2x - 1 - \sin(3\pi x)/6 & \text{otherwise,} \end{cases} \tag{82}$$

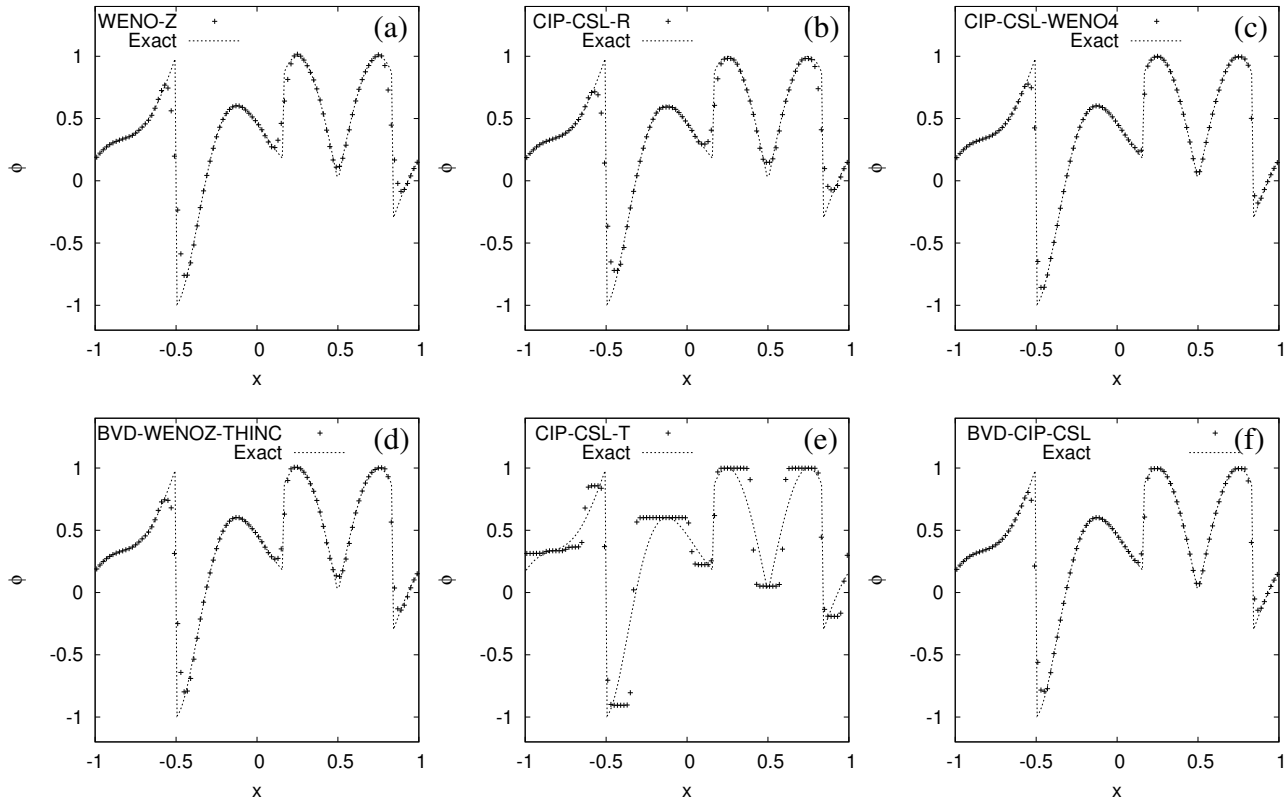

Figure 4: Numerical results of capturing extrema of various smoothness test at t=2. N=100 and CFL=0.4 are used. (a) WENO-Z, (b) CIP-CSL-R, (c) CIP-CSL-WENO4, (d) BVD-WENOZ-THINC, (e) CIP-CSL-T, (f) BVD-CIP-CSL.

Table 5: Numerical errors in capturing extrema of various smoothness test at t=2. N=100 and CFL=0.4 are used.

	Total error	Dissipation error	Dispersion error	L_1 error	L_∞ error
WENO-Z	2.02×10^{-2}	2.70×10^{-3}	1.75×10^{-2}	5.08×10^{-2}	7.66×10^{-1}
CIP-CSL-R	1.27×10^{-2}	2.09×10^{-3}	1.06×10^{-2}	4.58×10^{-2}	6.19×10^{-1}
CIP-CSL-WENO4	5.84×10^{-3}	6.94×10^{-4}	5.14×10^{-3}	2.25×10^{-2}	4.90×10^{-1}
BVD-WENOZ-THINC	1.42×10^{-2}	1.52×10^{-3}	1.27×10^{-2}	4.07×10^{-2}	7.36×10^{-1}
CIP-CSL-T	3.42×10^{-2}	6.30×10^{-3}	2.79×10^{-2}	1.30×10^{-1}	6.18×10^{-1}
BVD-CIP-CSL	5.45×10^{-3}	5.48×10^{-4}	4.91×10^{-3}	2.19×10^{-2}	4.81×10^{-1}

Numerical results and errors at $t = 2$ (1 period) are shown in Fig. 4 and Table 5, respectively. It is found that the BVD-CIP-CSL scheme performs better than WENO-Z, CIP-CSL-R, CIP-CSL-WENO4, CIP-CSL-T, and BVD-WENOZ-THINC schemes. The results are consistent with the results of complex wave propagation test.

3.3.4. 2D Zalesak test

A rotated notched cylinder, which called the Zalesak's problem is widely used as a test for 2D scalar advection. In this paper, one revolution of Zalesak's problem is conducted on a Cartesian grid (100×100) with the velocity $\mathbf{u} = (y-0.5, 0.5-x)$ and $\Delta t = 2\pi/628$. The implementation of semi-Lagrangian schemes in multi-dimentional advection tests can be conducted by the Strang splitting method [62].

Table 6: Numerical errors in 2D Zalesak test at t=1, N=100×100.

	Total error	Dissipation error	Dispersion error	L_1 error	L_∞ error
WENO-Z	3.86×10^{-3}	3.62×10^{-4}	3.49×10^{-3}	1.32×10^{-2}	6.98×10^{-1}
CIP-CSL-WENO4	1.33×10^{-3}	1.40×10^{-4}	1.19×10^{-3}	7.65×10^{-3}	3.77×10^{-1}
BVD-WENOZ-THINC	2.86×10^{-3}	8.08×10^{-4}	2.05×10^{-3}	7.79×10^{-3}	8.40×10^{-1}
BVD-CIP-CSL	1.13×10^{-3}	1.09×10^{-4}	1.02×10^{-3}	6.83×10^{-3}	3.63×10^{-1}

Fig. 5 and Table 6 show numerical results and errors of WENO-Z, CIP-CSL-WENO4, BVD-WENOZ-THINC, and BVD-CIP-CSL schemes in top view. It is observed that BVD-CIP-CSL produces the least numerical errors compared to other schemes, suggesting BVD-CIP-CSL scheme can resolve the shape of 2D advection problem accurately.

3.4. Burgers' equation

In this test, we evaluate the proposed scheme by solving the nonlinear inviscid Burgers' equation [63] in its conservative formulation as follows

$$\frac{\partial u}{\partial t} + \frac{\partial (u^2/2)}{\partial x} = 0. \tag{83}$$

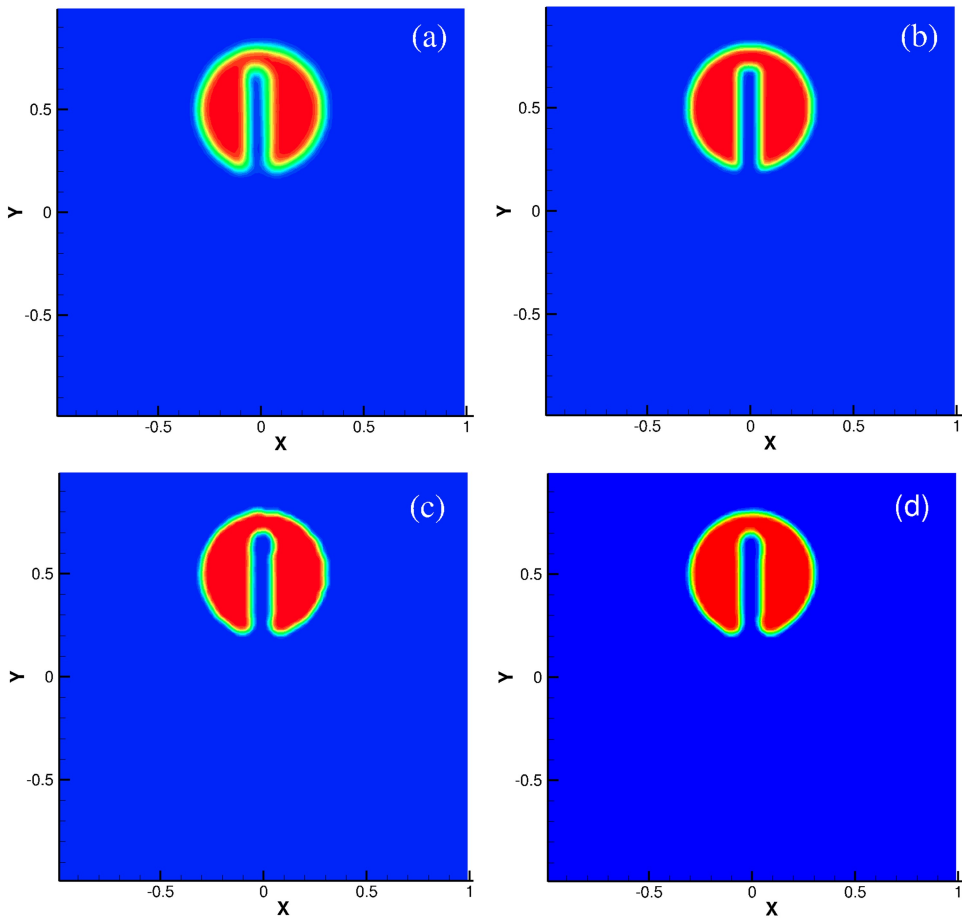

Figure 5: Numerical results of 2D Zalesak test at t=1, N=100 × 100. (a) WENO-Z, (b) CIP-CSL-WENO4, (c) BVD-WENOZ-THINC, (d) BVD-CIP-CSL, top views.

The numerical mesh size is $N = 100$, the computational domain $0 \leq x \leq 2$ and periodic boundary conditions are used. The initial condition of velocity is given as $u(x,0) = \sin(\pi x)$. The reference solution is created by using CSL3CW [28] with a high resolution (10,000 cells).

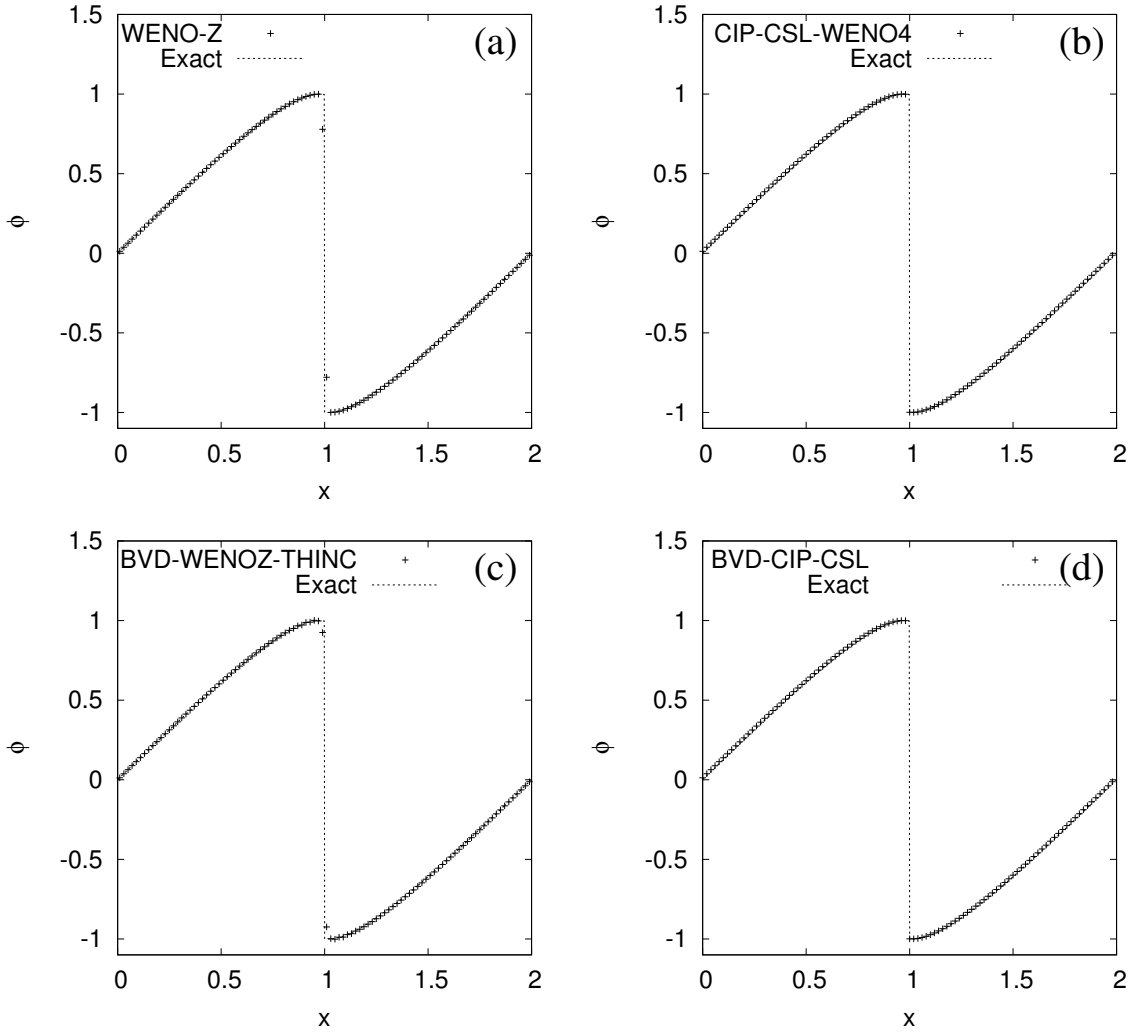

Figure 6: Numerical results of Burgers' equation at t=1.5/π. N=100 and CFL=0.2 are used. (a) WENO-Z, (b) CIP-CSL-WENO4, (c) BVD-WENOZ-THINC, (d) BVD-CIP-CSL.

Numerical results at time $t = 1.5/\pi$ are shown in Fig. 6. Results show that multi-moments schemes (icluding CIP-CSL-WENO4 and BVD-CIP-CSL) capture discontinuities well with less numerical dissipation compared to single moment finite volume schemes (including WENO-Z and BVD-WENOZ-THINC).

3.5. Euler equation

In this section, we validate the proposed scheme by solving inviscid Euler conservation equations, including Sod's problem, Lax's problem, shock-turbulence interaction problem and two blast wave interaction problem. Exact solutions

are obtained by using VSIAM3 [16] with a high numerical resolution (10,000 cells).

3.5.1. Sod's problem

Sod's problem [64] is one of the most widely used benchmark test for one-dimensional Euler equations. The initial conditions are given as follows

$$\begin{aligned} &\rho(x,0)=1; \quad && u(x,0)=0; \quad && p(x,0)=1; \quad && \text{if } x<0.5 \\ &\rho(x,0)=0.125; \quad && u(x,0)=0; \quad && p(x,0)=0.1; \quad && \text{otherwise,} \end{aligned} \tag{84}$$

where ρ is density and p is pressure. We carry out the numerical simulation with the mesh size $N=100$ until time at $t=0.2$.

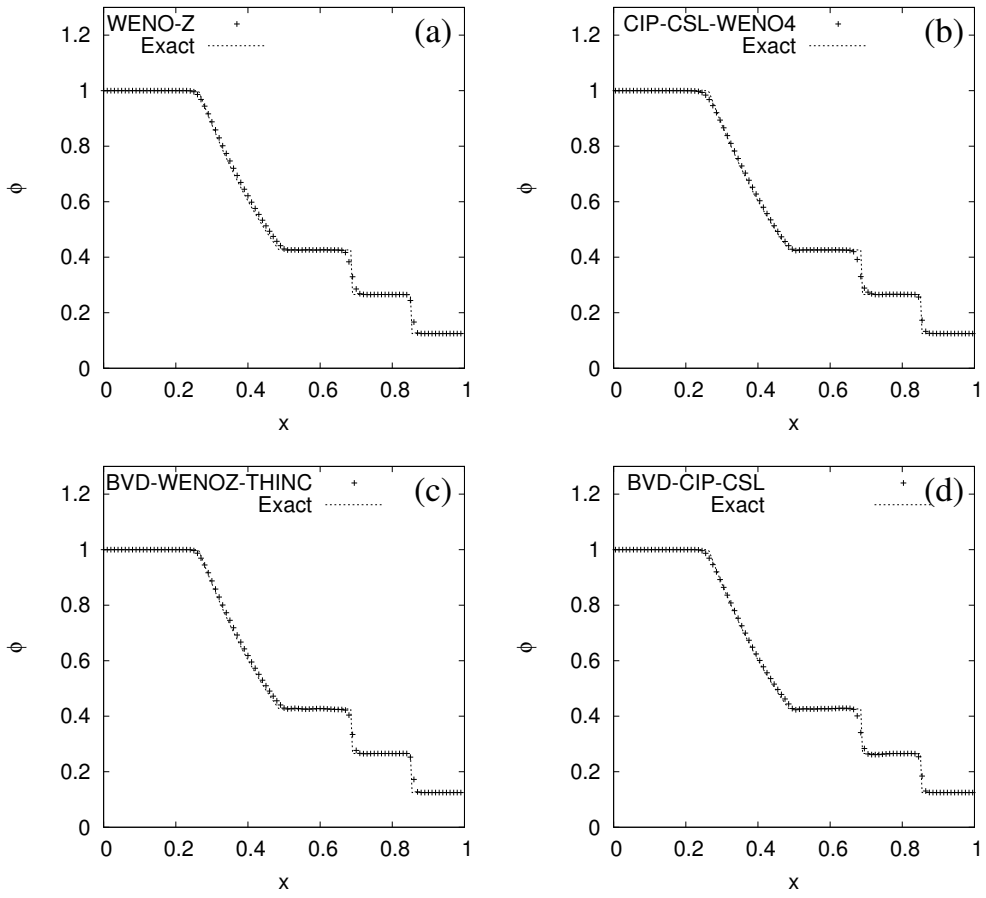

Figure 7: Numerical results of Sod's shock tube problem at t = 0.2 and N=100. (a) WENO-Z, (b) CIP-CSL-WENO4, (c) BVD-WENOZ-THINC, (d) BVD-CIP-CSL.

Fig. 7 shows the numerical results, it is observed that WENO-Z, CIP-CSL-WENO4, BVD-WENOZ-THINC, and BVD-CIP-CSL capture shock well without oscillation. In discontinuity region, both BVD-WENOZ-THINC and BVD-CIP-CSL schemes perform better than WENO-Z and CIP-CSL-WENO4 schemes.

3.5.2. Lax's problem

In Lax's problem [65], a numerical test with strong shock and contact discontinuity which is characterized by the following initial condition

$$\begin{aligned} &\rho(x,0) = 0.445; \quad u(x,0) = 0.698; \quad p(x,0) = 3.528; \quad \text{if } x < 0.5 \\ &\rho(x,0) = 0.5; \qquad u(x,0) = 0; \qquad\quad p(x,0) = 0.571; \quad \text{otherwise,} \end{aligned} \tag{85}$$

The numerical mesh size $N = 100$ is performed. Fig. 8 shows numerical results at time t=0.16.

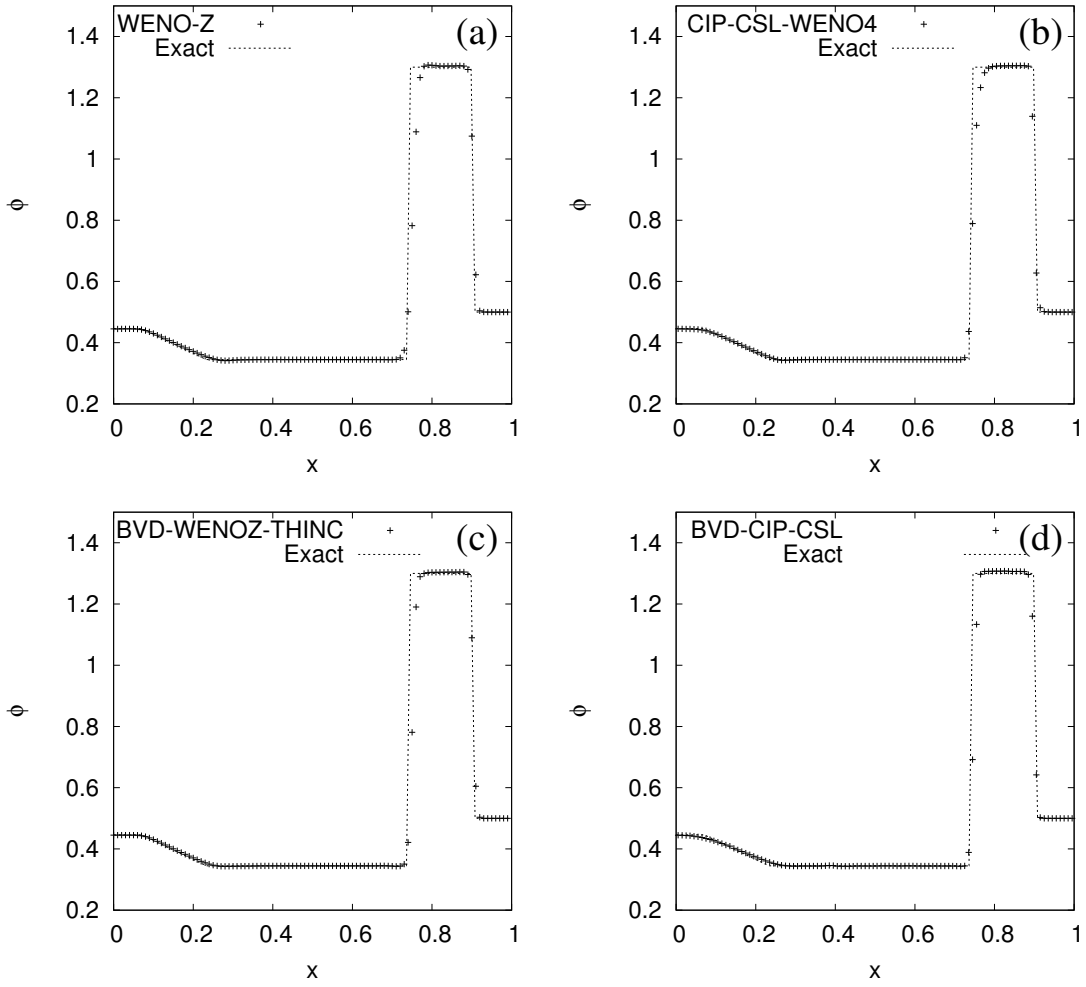

Figure 8: Numerical results of Lax's shock tube problem at t=0.16 and N=100. (a) WENO-Z, (b) CIP-CSL-WENO4, (c) BVD-WENOZ-THINC, (d) BVD-CIP-CSL.

It is observed that both BVD-WENOZ-THINC and BVD-CIP-CSL schemes reduce numerical dissipation in the discontinuous region compared with WENOZ and CIP-CSL-WENO4 scheme. This observation is consistent with the results of Sod's problem.

3.5.3. Shock turbulence interaction problem

In this test, we conduct the numerical simulation of the shock-turbulence interaction problem [31]. Interactions between a shock wave and perturbations are simulated with the following initial condition

$$\begin{array}{llll} \rho(x,0) = 3.857148; & u(x,0) = 2.629369; & p(x,0) = 10.333333; & \text{if } 0 \le x < 1 \\ \rho(x,0) = 1 + 0.2\sin(5x-5); & u(x,0) = 0; & p(x,0) = 1; & \text{otherwise.} \end{array} \tag{86}$$

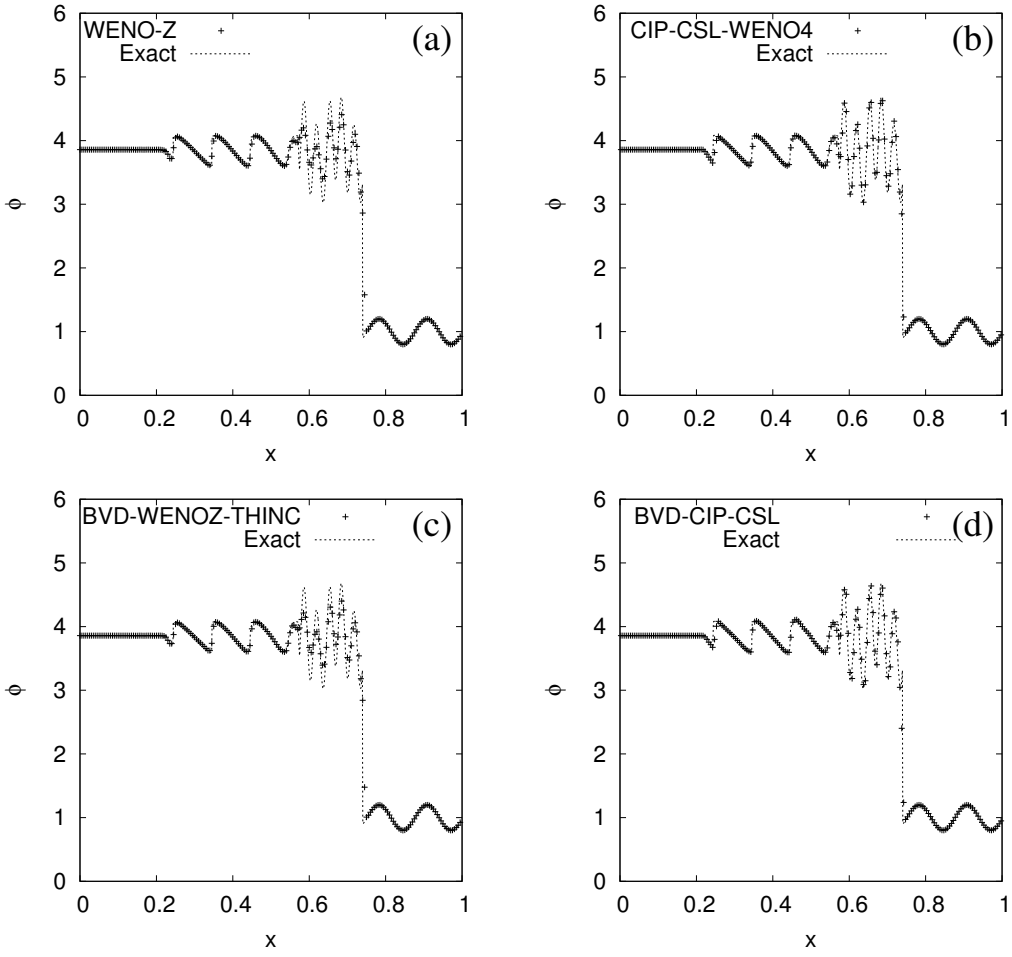

Figure 9: Numerical results of shock-turbulence interaction problem at t=0.18 and N=200. (a) WENO-Z, (b) CIP-CSL-WENO4, (c) BVD-WENOZ-THINC, (d) BVD-CIP-CSL.

Fig. 9 shows numerical results at t=0.18. We can observe that the proposed BVD-CIP-CSL scheme can capture discontinuities, high and low frequency wave profiles without numerical oscillations and less numerical dissipation. It is also found that high-frequency flow structure is smeared out by using WENO-Z and BVD-WENOZ-THINC, while CIP-CSL-WENO4 and BVD-CIP-CSL perform better than WENO-Z and BVD-WENOZ-THINC, respectively. This indicates that the proposed scheme based on multi-moments framework has high resolution property to solve complex flow structures especially for shock-turbulence interaction problems.

3.5.4. Two blast waves interaction problem

We also test the proposed schemes through two interacting blast waves simulation that was suggested in [65] with the following initial condition

$$(\rho_0, u_0, p_0) = \begin{cases} (1, 0, 1000) & \text{for} \quad 0 \leq x < 0.1 \\ (1, 0, 0.01) & \text{for} \quad 0.1 \leq x <= 0.9 \\ (1, 0, 100) & \text{otherwise,} \end{cases} \tag{87}$$

A numerical mesh size $N = 400$ and a reflecting boundary condition is used.

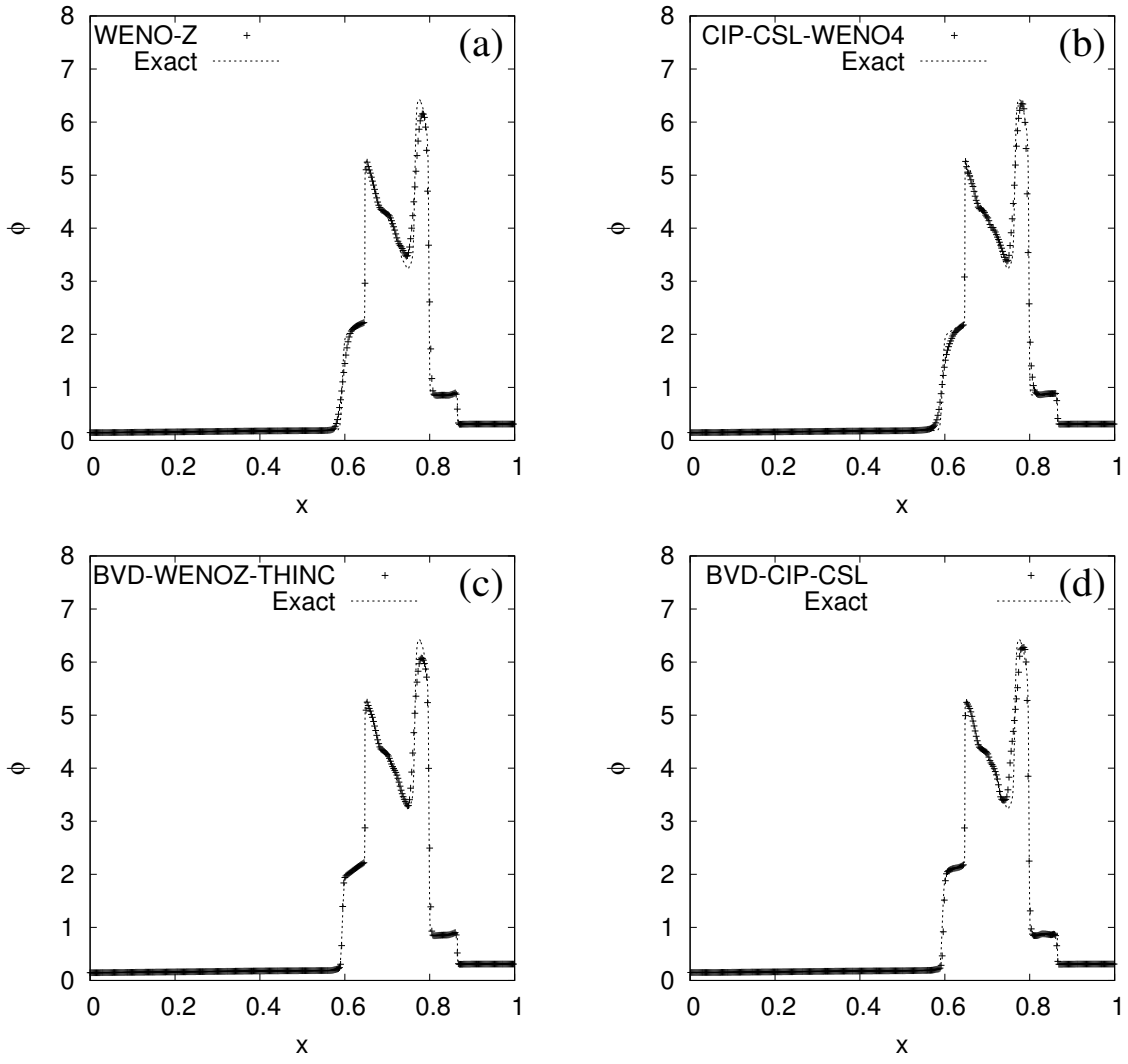

Figure 10: Numerical results of two interacting blasting waves problem at t=0.038 and N=400. (a) WENO-Z, (b) CIP-CSL-WENO4, (c) BVD-WENOZ-THINC, (d) BVD-CIP-CSL.

In this test, two blast waves are formed by the initial jumps. Expansion fans, contact discontinuities and strong shocks are generated and interact with each other. Due to violent interactions, the existence of oscillation may cause

a break up of the simulation. Another difficulty for existing shock-capturing schemes is the overly smeared density discontinuities in the numerical solution [36].

The results at time $t = 0.038$ are shown in Fig. 10. It is observed that the left-most density discontinuity is smeared in the numerical solution of WENO-Z and CIP-CSL-WENO4. Both BVD-WENOZ-THINC and BVD-CIP-CSL reduce the numerical dissipation in the vicinity of the density discontinuity effectively. In terms of capturing the shock, BVD-CIP-CSL performs better than the BVD-WENOZ-THINC scheme.

3.5.5. 2D lid-driven cavity flow problem

To further verify the proposed method in the simulation of incompressible viscous flows, we conduct a widely used benchmark test, which is called lid-driven cavity flow test. In this paper, numerical simulations with Reynolds numbers 1000 and 3200 respectively are conducted on a Cartesion grid (100×100). The computation domain is $[0,1][0,1]$ with a driving velocity of the upper lid $u = 1$.

Results of horizontal velocity component u along the $x = 0.5$ axis and the vertical velocity component v along the $y = 0.5$ axis with two different Reynolds number are shown in Fig. 11. We compare the numerical result against the result in [66]. It can be observed that the velocity components are accurately simulated using the proposed BVD-CIP-CSL scheme, suggesting the proposed scheme is capable of simulating incompressible flows faithfully.

3.5.6. 2D circular explosion problem

To validate the proposed method in the simulation of compressible flows, the numerical simulation of a circular two-dimensional explosion of inviscid compressible flows is tested. The computation domain is $[-1,1][-1,1]$ and the initial conditions are given as follows

$$(\rho,u,v,p) = \begin{cases} (1,0,0,1) & \text{for} \quad r \leq 0.5 \\ (0.125,0,0,0.1) & \text{otherwise,} \end{cases} \tag{88}$$

where the radius $r = \sqrt{x^2+y^2}$. With these initial conditions, an axis-symmetric explosion configuration that contains rarefraction wave, contact discontinuity and shock waves is formed.

Fig.12 left shows the side view of the density profile at time $t = 0.25$ on a 400×400 Cartesian grids. Fig.12 right shows the density along the cross-section of $x = y$, against with the reference solution created by using VSIAM3 scheme[17] with a high numerical resolution (10,000 cells). It can be observed that shock, contact discontinuity and the rarefaction wave are well simulated by the proposed BVD-CIP-CSL scheme. This indicates that BVD-CIP-CSL scheme has significant potential to simulate compressible flows.

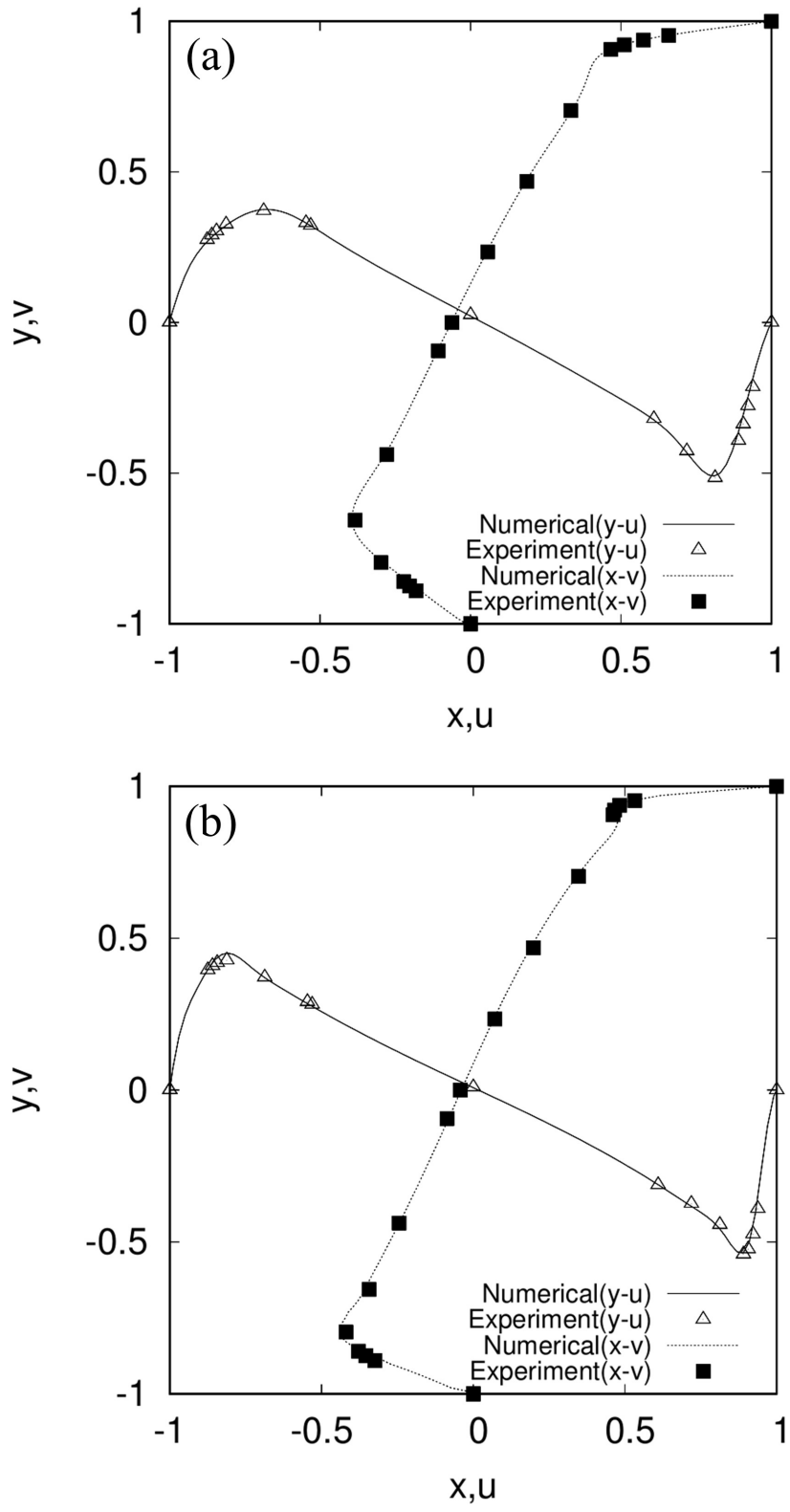

Figure 11: The horizontal velocity component u along the $x = 0.5$ axis and the vertical velocity component v along the $y = 0.5$ axis. Displayed are the results of BVD-CIP-CSL scheme on a 100×100 meshs with the Reynolds number being 1000 (a) and 3200 (b) respectively.

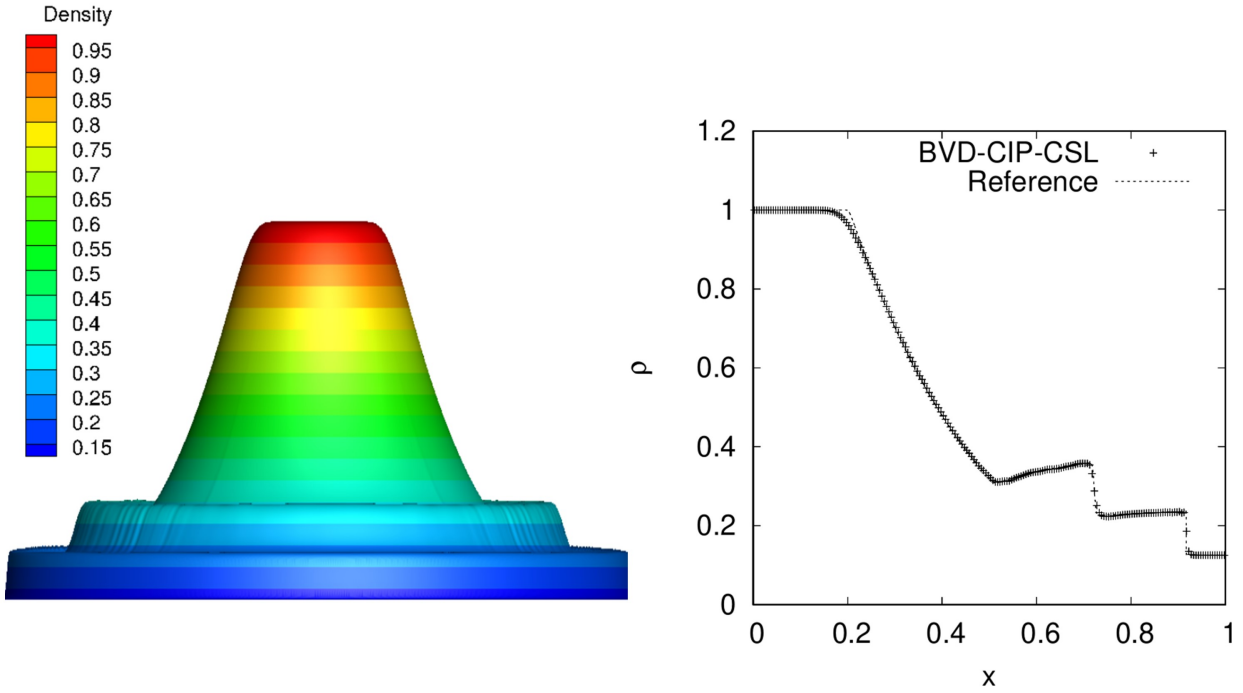

Figure 12: 2D-circular explosion of BVD-CIP-CSL scheme at t=0.25. The density profile, side view (left) and the density profile along the cross-section of $x = y$ (right).

4. Conclusions and future work

In this paper, the BVD-CIP-CSL scheme was proposed based on the CIP-CSL-WENO4 scheme and a newly designed CIP-CSL-T scheme. In CIP-CSL-T scheme, a piecewise tangent hyperbolic function is implemented into the CIP-CSL framework to reduce the numerical errors in the vicinity of discontinuities. For smooth solutions, the fourth-order CIP-CSL-WENO4 scheme is used as another candidate. The reconstruction criterion of the BVD-CIP-CSL scheme is designed based on a modified version of boundary variation diminishing algorithm, which can minimize the total boundary variations of the derivative at cell boundaries. The proposed BVD-CIP-CSL scheme has been verified through a variety of numerical benchmark tests in comparison with other high-order CIP-CSL and WENO schemes. Numerical results show that the BVD-CIP-CSL scheme effectively reduce numerical errors for smooth solutions and minimize numerical diffusion in the vicinity of discontinuities. The performance of the proposed method is convincingly verified with several benchmarks tests, which justify that the BVD-CIP-CSL is superior to other existing methods of the same order in terms of numerical dissipation errors. In addition, the proposed BVD-CIP-CSL scheme was successfully applied to simulate both compressible and incompressible flows by implementing a unified pressure based fractional step procedure. Numerical results of 2D lid-driven cavity and 2D explosion tests show that the proposed scheme can accurately simulate both incompressible and compressible flows. This suggests that the BVD-CIP-CSL scheme has great potential to be an effective and practical approach in the simulation of complex flow problems where

both compressible and incompressible flows exist and the physical dissipation plays an important role.

It has been demonstrated in previous papers that multi-moment methods have been successfully extend to 3D calculation and achieve more accurate and robust than conventional finite volume method [58–60]. Based on the preliminary results of the proposed method, we see an essential future work to extend this algorithm to 3D complex phenomena such as Taylor Green vortex problem, which involves transition to turbulence followed by dissipation.

Acknowledgments

This research work was supported by the National Natural Science Foundation of China (Grant Nos. 51725902, 41890820); the Royal Academy of Engineering through the Urban Flooding Research Policy Impact Programme (Grant No. UUFRIP/100031); and the Newton Advanced Fellowships from the NSFC and the UK Royal Society (Grant Nos. 52061130219; NAF/R1/201156). This research was also supported in part by FLEXIS which is part-funded by the European Regional Development Fund (ERDF), through the Welsh Government. The authors would like to express their sincere thanks to the editor and anonymous referees for their valuable comments and suggestions.

Data availability

The data that support the findings of this study are available from the corresponding author upon reasonable request.

References

[1] S. M. Safdari, O. Mahian, M. H. Doranehgard, Special topic on turbulent and multiphase flows, Physics of Fluids 33 (9) (2021) 090401 (2021). arXiv:https://doi.org/10.1063/5.0066618, doi:10.1063/5.0066618.
URL https://doi.org/10.1063/5.0066618

[2] K. Zhang, S. Hayostek, M. Amitay, W. He, V. Theofilis, K. Taira, On the formation of three-dimensional separated flows over wings under tip effects, Journal of Fluid Mechanics 895 (2020) A9 (2020). doi:10.1017/jfm.2020.248.

[3] M. Doosttalab, O. Frommann, Multidisciplinary design and verification of the hb flatback airfoil family, AIAA Journal 57 (11) (2019) 4639–4649 (2019). arXiv:https://doi.org/10.2514/1.J057684, doi:10.2514/1.J057684.
URL https://doi.org/10.2514/1.J057684

[4] M. Dellacasagrande, D. Lengani, D. Simoni, J. O. Pralits, K. Durovich, A. Hanifi, D. Henningson, Statistical characterization of free-stream turbulence induced transition under variable reynolds number, free-stream turbulence, and pressure gradient, Physics of Fluids 33 (9) (2021) 094115 (2021). arXiv:https://doi.org/10.1063/5.0063948, doi:10.1063/5.0063948.
URL https://doi.org/10.1063/5.0063948

[5] A. Broatch, R. Novella, J. García-Tíscar, J. Gomez-Soriano, P. Pal, Analysis of combustion acoustic phenomena in compression–ignition engines using large eddy simulation, Physics of Fluids 32 (8) (2020) 085101 (2020). arXiv:https://doi.org/10.1063/5.0011929, doi:10.1063/5.0011929.
URL https://doi.org/10.1063/5.0011929

[6] Z. Du, W. Huang, L. Yan, S. Li, Reynolds-average navier-stokes study of steady and pulsed gaseous jets with different periods for the shock-induced combustion ramjet engine, Physics of Fluids 31 (5) (2019) 055107 (2019). arXiv:https://doi.org/10.1063/1.5097238, doi:10.1063/1.5097238.
URL https://doi.org/10.1063/1.5097238

[7] S. Shima, K. Nakamura, H. Gotoda, Y. Ohmichi, S. Matsuyama, Formation mechanism of high-frequency combustion oscillations in a model rocket engine combustor, Physics of Fluids 33 (6) (2021) 064108 (2021). arXiv:https://doi.org/10.1063/5.0048785, doi:10.1063/5.0048785.
URL https://doi.org/10.1063/5.0048785

[8] Z. Li, Y. Ju, C. Zhang, Parallel large eddy simulations of transitional flow in a compressor cascade with endwalls, Physics of Fluids 31 (11) (2019) 115104 (2019). arXiv:https://doi.org/10.1063/1.5123034, doi:10.1063/1.5123034.
URL https://doi.org/10.1063/1.5123034

[9] A. Sengupta, P. Tucker, Effects of forced frequency oscillations and free stream turbulence on the separation-induced transition in pressure gradient dominated flows, Physics of Fluids 32 (10) (2020) 104105 (2020). arXiv:https://doi.org/10.1063/5.0022865, doi:10.1063/5.0022865.
URL https://doi.org/10.1063/5.0022865

[10] M. Manolesos, G. Papadakis, Investigation of the three-dimensional flow past a flatback wind turbine airfoil at high angles of attack, Physics of Fluids 33 (8) (2021) 085106 (2021). arXiv:https://doi.org/10.1063/5.0055822, doi:10.1063/5.0055822.
URL https://doi.org/10.1063/5.0055822

[11] P. Samuthira, S. Jawahar, S. Mittal, Wake transitions and laminar separation bubble in the flow past an eppler 61 airfoil, Physics of Fluids 31 (11) (2019) 114102 (2019). arXiv:https://doi.org/10.1063/1.5113823, doi:10.1063/1.5113823.
URL https://doi.org/10.1063/1.5113823

[12] P. Reinke, M. Schmidt, T. Beckmann, The cavitating taylor-couette flow, Physics of Fluids 30 (10) (2018) 104101 (2018). arXiv:https://doi.org/10.1063/1.5049743, doi:10.1063/1.5049743.
URL https://doi.org/10.1063/1.5049743

[13] X. Zhang, M. Ge, G. Zhang, C. D. Oliver, Compressible effects modeling for turbulent cavitating flow in a small venturi channel: An empirical turbulent eddy viscosity correction, Physics of Fluids 33 (3) (2021) 035148 (2021).

arXiv:https://doi.org/10.1063/5.0041463, doi:10.1063/5.0041463.
URL https://doi.org/10.1063/5.0041463

[14] S. Yang, C. Habchi, Real-fluid phase transition in cavitation modeling considering dissolved non-condensable gas, Physics of Fluids 32 (3) (2020) 032102 (2020). arXiv:https://doi.org/10.1063/1.5140981, doi:10.1063/1.5140981.
URL https://doi.org/10.1063/1.5140981

[15] E. Kadivar, M. V. Timoshevskiy, M. Y. Nichik, O. el Moctar, T. E. Schellin, K. S. Pervunin, Control of unsteady partial cavitation and cloud cavitation in marine engineering and hydraulic systems, Physics of Fluids 32 (5) (2020) 052108 (2020). arXiv:https://doi.org/10.1063/5.0006560, doi:10.1063/5.0006560.
URL https://doi.org/10.1063/5.0006560

[16] F. Xiao, Unified formulation for compressible and incompressible flows by using multi-integrated moments i: one-dimensional inviscid compressible flow, Journal of Computational Physics 195 (2) (2004) 629–654 (2004). doi:https://doi.org/10.1016/j.jcp.2003.10.014.
URL https://www.sciencedirect.com/science/article/pii/S002199910300576X

[17] F. Xiao, R. Akoh, S. Ii, Unified formulation for compressible and incompressible flows by using multi-integrated moments II: Multi-dimensional version for compressible and incompressible flows, Journal of Computational Physics 213 (1) (2006) 31 – 56 (2006). doi:http://dx.doi.org/10.1016/j.jcp.2005.08.002.
URL http://www.sciencedirect.com/science/article/pii/S002199910500358X

[18] B. Xie, X. Deng, Z. Sun, F. Xiao, A hybrid pressure-density-based mach uniform algorithm for 2d euler equations on unstructured grids by using multi-moment finite volume method, Journal of Computational Physics 335 (2017) 637 – 663 (2017).

[19] L. Zhang, Z. Chen, L. Yang, C. Shu, An improved discrete gas-kinetic scheme for two-dimensional viscous incompressible and compressible flows, Physics of Fluids 31 (6) (2019) 066103 (2019). arXiv:https://doi.org/10.1063/1.5103229, doi:10.1063/1.5103229.
URL https://doi.org/10.1063/1.5103229

[20] Y. Zhu, C. Zhong, K. Xu, Unified gas-kinetic scheme with multigrid convergence for rarefied flow study, Physics of Fluids 29 (9) (2017) 096102 (2017). arXiv:https://doi.org/10.1063/1.4994020, doi:10.1063/1.4994020.
URL https://doi.org/10.1063/1.4994020

[21] Y. Zhu, C. Zhong, K. Xu, An implicit unified gas-kinetic scheme for unsteady flow in all knudsen regimes, Journal of Computational Physics 386 (2019) 190–217 (2019). doi:https://doi.org/10.1016/j.jcp.

2019.01.033.
URL https://www.sciencedirect.com/science/article/pii/S0021999119300841

[22] L. Yang, C. Shu, Y. Wang, Y. Sun, Development of discrete gas kinetic scheme for simulation of 3d viscous incompressible and compressible flows, Journal of Computational Physics 319 (2016) 129–144 (2016). doi:https://doi.org/10.1016/j.jcp.2016.05.018.
URL https://www.sciencedirect.com/science/article/pii/S0021999116301553

[23] L. M. Yang, C. Shu, Y. Wang, Development of a discrete gas-kinetic scheme for simulation of two-dimensional viscous incompressible and compressible flows, Phys. Rev. E 93 (2016) 033311 (Mar 2016). doi:10.1103/PhysRevE.93.033311.
URL https://link.aps.org/doi/10.1103/PhysRevE.93.033311

[24] X. Nogueira, L. Ramírez, S. Khelladi, J. C. Chassaing, I. Colominas, A high-order density-based finite volume method for the computation of all-speed flows, Computer Methods in Applied Mechanics and Engineering 298 (2016) 229–251 (2016). doi:https://doi.org/10.1016/j.cma.2015.10.004.
URL https://www.sciencedirect.com/science/article/pii/S0045782515003230

[25] C. M. Xisto, J. C. Páscoa, P. J. Oliveira, D. A. Nicolini, A hybrid pressure–density-based algorithm for the euler equations at all mach number regimes, International Journal for Numerical Methods in Fluids 70 (8) (2012) 961–976 (2012). arXiv:https://onlinelibrary.wiley.com/doi/pdf/10.1002/fld.2722, doi:https://doi.org/10.1002/fld.2722.
URL https://onlinelibrary.wiley.com/doi/abs/10.1002/fld.2722

[26] T. Yabe, R. Tanaka, T. Nakamura, F. Xiao, An exactly conservative semi-lagrangian scheme (CIP-CSL) in one dimension, Monthly Weather Review 129 (2) (2001) 332–344 (2001).

[27] T. Yabe, F. Xiao, T. Utsumi, The constrained interpolation profile method for multiphase analysis, Journal of Computational Physics 169 (2) (2001) 556 – 593 (2001). doi:http://dx.doi.org/10.1006/jcph.2000.6625.
URL http://www.sciencedirect.com/science/article/pii/S0021999100966257

[28] F. Xiao, T. Yabe, Completely conservative and oscillationless semi-lagrangian schemes for advection transportation, Journal of computational physics 170 (2) (2001) 498–522 (2001).

[29] F. Xiao, T. Yabe, X. Peng, H. Kobayashi, Conservative and oscillation-less atmospheric transport schemes based on rational functions, Journal of Geophysical Research: Atmospheres 107 (D22) (2002) 1–11 (2002).

[30] A. Harten, B. Engquist, S. Osher, S. R. Chakravarthy, Uniformly high order accurate essentially non-oscillatory schemes, iii, Journal of Computational Physics 131 (1) (1997) 3 – 47 (1997). doi:https://doi.org/10.1006/jcph.1996.5632.
URL http://www.sciencedirect.com/science/article/pii/S0021999196956326

[31] C. Shu, S. Osher, Efficient implementation of essentially non-oscillatory shock-capturing schemes, Journal of Computational Physics 77 (2) (1988) 439 – 471 (1988). doi:https://doi.org/10.1016/0021-9991(88)90177-5.
URL http://www.sciencedirect.com/science/article/pii/0021999188901775

[32] Q. Li, S. Omar, X. Deng, K. Yokoi, Constrained interpolation profile conservative semi-lagrangian scheme based on third-order polynomial functions and essentially non-oscillatory (cip-csl3eno) scheme, Communications in Computational Physics 22 (3) (2017) 765–788 (2017).

[33] Z. Sun, F. Xiao, A semi-lagrangian multi-moment finite volume method with fourth-order weno projection, International Journal for Numerical Methods in Fluids 83 (4) (2017) 351–375 (2017). arXiv:https://onlinelibrary.wiley.com/doi/pdf/10.1002/fld.4271, doi:10.1002/fld.4271.
URL https://onlinelibrary.wiley.com/doi/abs/10.1002/fld.4271

[34] G. Jiang, C. Shu, Efficient implementation of weighted eno schemes, Journal of Computational Physics 126 (1) (1996) 202 – 228 (1996). doi:https://doi.org/10.1006/jcph.1996.0130.
URL http://www.sciencedirect.com/science/article/pii/S0021999196901308

[35] R. Borges, M. Carmona, B. Costa, W. S. Don, An improved weighted essentially non-oscillatory scheme for hyperbolic conservation laws, Journal of Computational Physics 227 (6) (2008) 3191 – 3211 (2008). doi:https://doi.org/10.1016/j.jcp.2007.11.038.
URL http://www.sciencedirect.com/science/article/pii/S0021999107005232

[36] Z. Sun, S. Inaba, F. Xiao, Boundary variation diminishing (bvd) reconstruction: A new approach to improve godunov schemes, Journal of Computational Physics 322 (2016) 309 – 325 (2016). doi:https://doi.org/10.1016/j.jcp.2016.06.051.
URL http://www.sciencedirect.com/science/article/pii/S0021999116302765

[37] X. Deng, S. Inab, B. Xie, K. M. Shyue, F. Xiao, High fidelity discontinuity-resolving reconstruction for compressible multiphase flows with moving interfaces, Journal of Computational Physics 371 (2018) 945 – 966 (2018).

[38] X. Deng, Y. Shimizu, F. Xiao, A fifth-order shock capturing scheme with two-stage boundary variation diminishing algorithm, Journal of Computational Physics 386 (2019) 323 – 349 (2019).

[39] X. Deng, B. Xie, R. Loubère, Y. Shimizu, F. Xiao, Limiter-free discontinuity-capturing scheme for compressible gas dynamics with reactive fronts, Computers and Fluids 171 (2018) 1 – 14 (2018).

[40] X. Deng, B. Xie, R. Loubère, Y. Shimizu, F. Xiao, A new shock-capturing scheme for stiff detonation waves problems, AIAA 56 (2018) 1 – 20 (2018).

[41] X. Deng, Y. Shimizu, B. Xie, F. Xiao, Constructing higher order discontinuity-capturing schemes with upwind-biased interpolations and boundary variation diminishing algorithm, Computers and Fluids 200 (2020) 104433

(2020). doi:https://doi.org/10.1016/j.compfluid.2020.104433.
URL https://www.sciencedirect.com/science/article/pii/S0045793020300098

[42] Q. Li, K. Yokoi, Z. Xie, S. Omar, J. Xue, A fifth-order high-resolution shock-capturing scheme based on modified weighted weighted essentially non-oscillatory method and boundary variation diminishing framework for compressible flows and compressible two-phase flows, Physics of fluids 33 (5) (2021) 056104 (2021). doi:https://doi.org/10.1063/5.0045635.

[43] F. Xiao, Y. Honma, T. Kono, A simple algebraic interface capturing scheme using hyperbolic tangent function, International Journal for Numerical Methods in Fluids 48 (9) (2005) 1023–1040 (2005).

[44] F. Xiao, S. Ii, C. Chen, Revisit to the THINC scheme: a simple algebraic VOF algorithm, Journal of Computational Physics 230 (19) (2011) 7086–7092 (2011).

[45] L. Cheng, X. Deng, B. Xie, Y. Jiang, F. Xiao, Low-dissipation bvd schemes for single and multi-phase compressible flows on unstructured grids, Journal of Computational Physics 428 (2021) 637 – 663 (2021).

[46] B. Xie, X. Feng, Toward efficient and accurate interface capturing on arbitrary hybrid unstructured grids: The thinc method with quadratic surface representation and gaussian quadrature, Journal of Computational Physics 349 (2017) 415–440 (2017).

[47] Z. Jiang, X. Deng, F. Xiao, C. Yan, J. Yu, A higher order interpolation scheme of finite volume method for compressible flow on curvilinear grids, Communications in Computational Physics 28 (4) (2020) 1609–1638 (2020). doi:https://doi.org/10.4208/cicp.OA-2019-0091.
URL http://global-sci.org/intro/article_detail/cicp/18190.html

[48] F. Xiao, T. Yabe, T. Ito, Constructing oscillation preventing scheme for advection equation by rational function, Computer Physics Communications 93 (1) (1996) 1–12 (1996).

[49] K. Shyue, F. Xiao, An Eulerian interface sharpening algorithm for compressible two-phase flow: The algebraic THINC approach, Journal of Computational Physics 268 (2014) 326–354 (2014).

[50] D. Cassidy, J. Edwards, M. Tian, An investigation of interface-sharpening schemes for multi-phase mixture flows, Journal of Computational Physics 228 (16) (2009) 5628–5649 (2009).

[51] X. Deng, B. Xie, R. Loubère, Y. Shimizu, F. Xiao, Limiter-free discontinuity-capturing scheme for compressible gas dynamics with reactive fronts, Computers & Fluids 171 (2018) 1 – 14 (2018). doi:https://doi.org/10.1016/j.compfluid.2018.05.015.
URL http://www.sciencedirect.com/science/article/pii/S0045793018302585

[52] C. Shu, Total-variation-diminishing time discretizations, SIAM Journal on Scientific and Statistical Computing 9 (6) (1988) 1073–1084 (1988).

[53] S. Ii, F. Xiao, CIP/multi-moment finite volume method for euler equations: A semi-lagrangian characteristic formulation, Journal of Computational Physics 222 (2) (2007) 849 – 871 (2007).

[54] K. Yokoi, M. Furuichi, M. Sakai, An efficient multi-dimensional implementation of vsiam3 and its applications to free surface flows, Physics of Fluids 29 (12) (2017) 121611 (2017).

[55] W. Gropp, E. Lusk, A. Skjellum, Using mpi portable parallel programming with the message-passing interface, in: Scientific and Engineering Computation Series, Massachusetts Institute of Technology, 2014 (2014).

[56] B. Xie, S. Ii, A. Ikebata, F. Xiao, A multi-moment finite volume method for incompressible navier–stokes equations on unstructured grids: Volume-average/point-value formulation, Journal of Computational Physics 277 (2014) 138–162 (2014). doi:https://doi.org/10.1016/j.jcp.2014.08.011.
URL https://www.sciencedirect.com/science/article/pii/S0021999114005579

[57] B. Xie, F. Xiao, Two and three dimensional multi-moment finite volume solver for incompressible navier–stokes equations on unstructured grids with arbitrary quadrilateral and hexahedral elements, Computers and Fluids 104 (2014) 40–54 (2014). doi:https://doi.org/10.1016/j.compfluid.2014.08.002.
URL https://www.sciencedirect.com/science/article/pii/S0045793014003260

[58] F. Xiao, B. Xie, Accurate and robust piso algorithm on hybrid unstructured grids using the multimoment finite volume method, Numerical Heat Transfer, Part B. Fundamentals: An International Journal of Computation and Methodology 71 (1/6) (2017) 146–172 (2017).

[59] B. Xie, S. Ii, F. Xiao, An efficient and accurate algebraic interface capturing method for unstructured grids in 2 and 3 dimensions: The thinc method with quadratic surface representation, International Journal for Numerical Methods in Fluids 76 (12) (2014) 1025–1042 (2014). arXiv:https://onlinelibrary.wiley.com/doi/pdf/10.1002/fld.3968, doi:https://doi.org/10.1002/fld.3968.
URL https://onlinelibrary.wiley.com/doi/abs/10.1002/fld.3968

[60] B. Xie, F. Xiao, A multi-moment constrained finite volume method on arbitrary unstructured grids for incompressible flows, Journal of Computational Physics 327 (2016) 747–778 (2016). doi:https://doi.org/10.1016/j.jcp.2016.09.054.
URL https://www.sciencedirect.com/science/article/pii/S0021999116304752

[61] L. L. Takacs, A two-step scheme for the advection equation with minimized dissipation and dispersion errors, Monthly Weather Review 113 (6) (1985) 1050–1065 (1985).

[62] G. Strang, On the construction and comparison of difference schemes, SIAM Journal on Numerical Analysis 5 (3) (1968) 506–517 (1968).

[63] J. Qiu, C. W. Shu, Hermite weno schemes and their application as limiters for runge–kutta discontinuous galerkin method: one-dimensional case, Journal of Computational Physics 193 (1) (2004) 115–135 (2004).

[64] G. A. Sod, A survey of several finite difference methods for systems of nonlinear hyperbolic conservation laws, Journal of computational physics 27 (1) (1978) 1–31 (1978).

[65] P. Woodward, P. Colella, The numerical simulation of two-dimensional fluid flow with strong shocks, Journal of computational physics 54 (1) (1984) 115–173 (1984).

[66] U. Ghia, K. N. Ghia, C. Shin, High resolutions for incompressible flow using the navier-stokes equations and a multigrid method, Journal of Computational Physics 48 (3) (1982) 387–411 (1982).

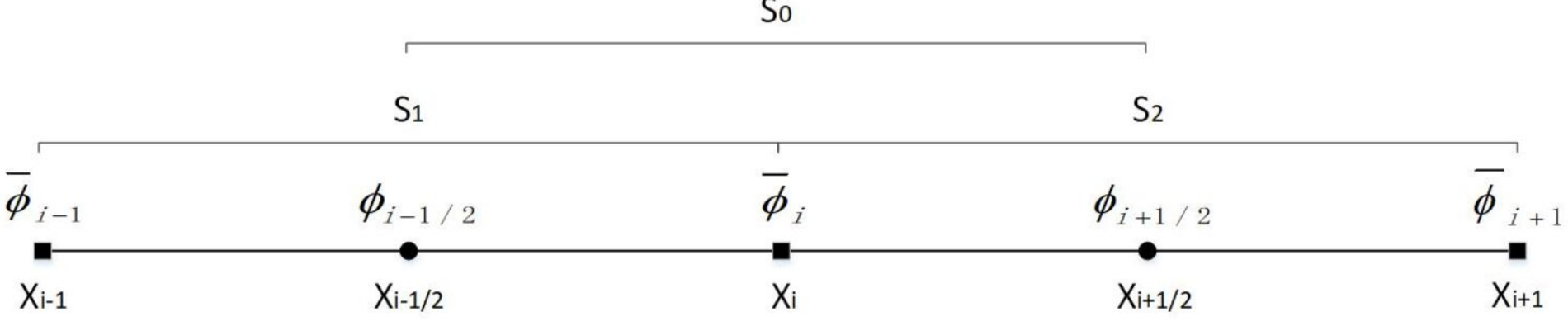
S0
S1
S2
$\overline{\phi}_{i-1}$
$\phi_{i-1/2}$
$\overline{\phi}_{i}$
$\phi_{i+1/2}$
$\overline{\phi}_{i+1}$
Xi-1
Xi-1/2
Xi
Xi+1/2
Xi+1

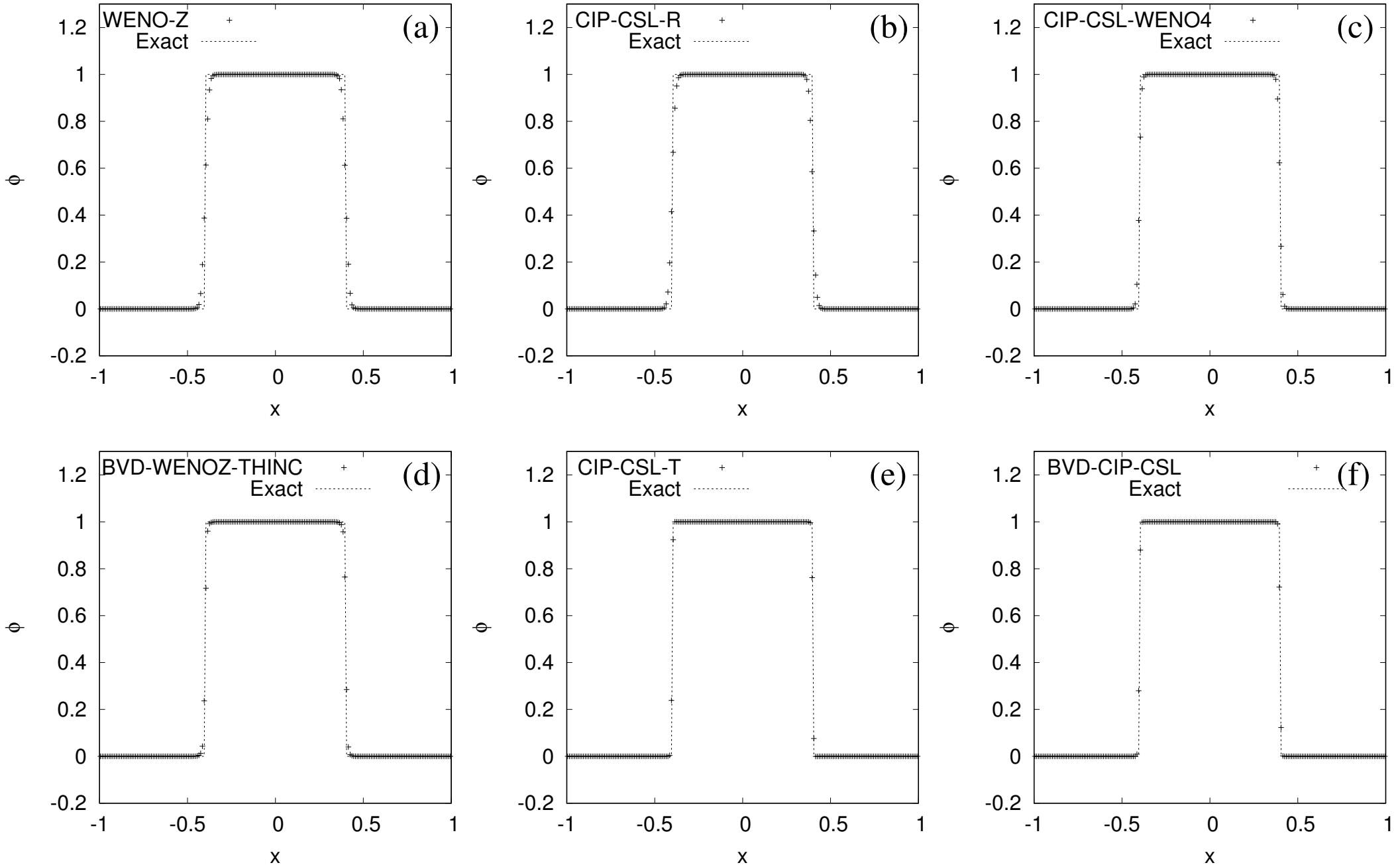
WENO-Z
Exact
(a)
CIP-CSL-R
Exact
(b)
CIP-CSL-WENO4
Exact
(c)
BVD-WENOZ-THINC
Exact
(d)
CIP-CSL-T
Exact
(e)
BVD-CIP-CSL
Exact
(f)
ϕ
x
1.2
1
0.8
0.6
0.4
0.2
0
-0.2
-1
-0.5
0
0.5
1

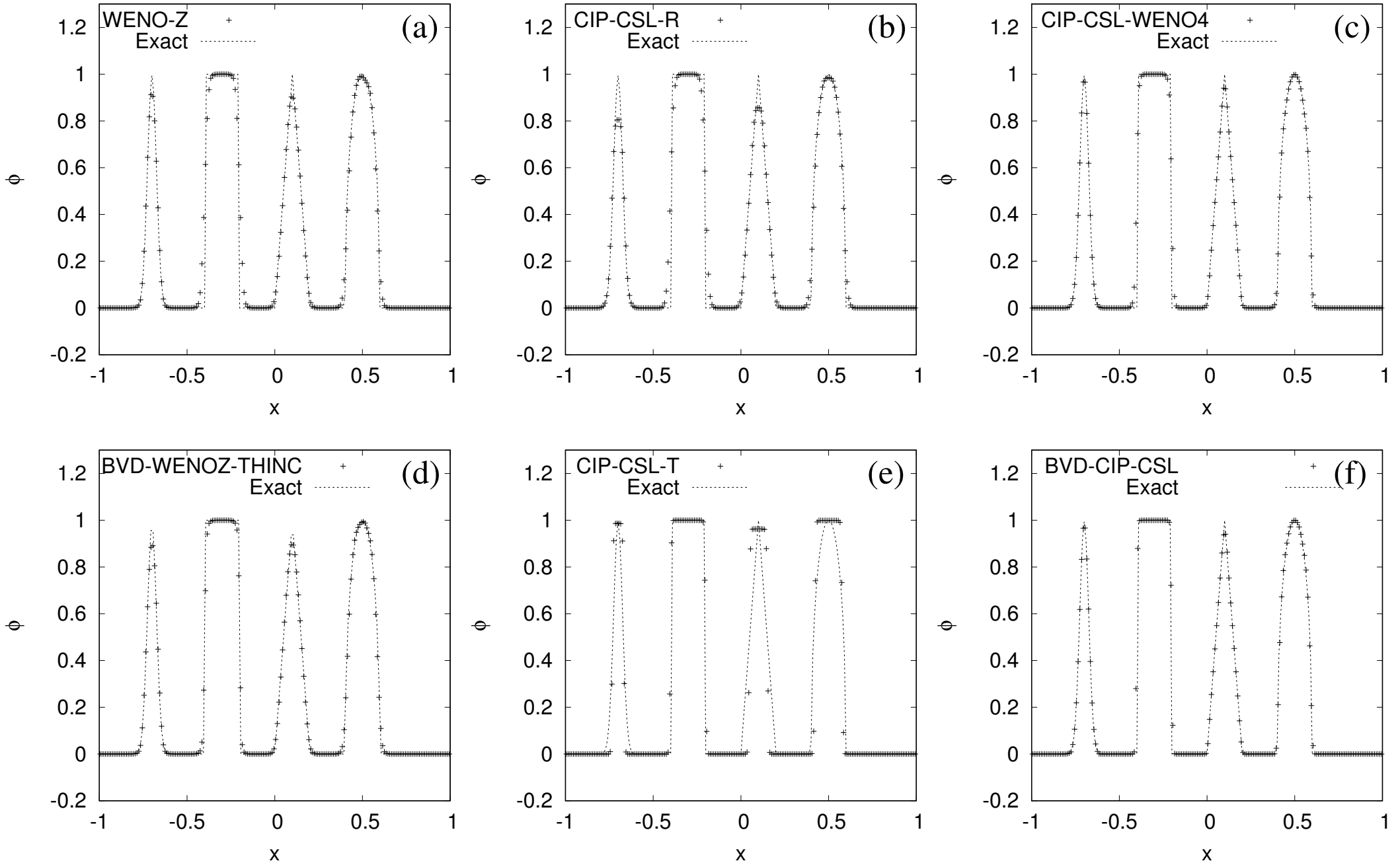
WENO-Z
Exact
(a)
CIP-CSL-R
Exact
(b)
CIP-CSL-WENO4
Exact
(c)
BVD-WENOZ-THINC
Exact
(d)
CIP-CSL-T
Exact
(e)
BVD-CIP-CSL
Exact
(f)
ϕ
x
1.2
1
0.8
0.6
0.4
0.2
0
-0.2
-1
-0.5
0
0.5
1

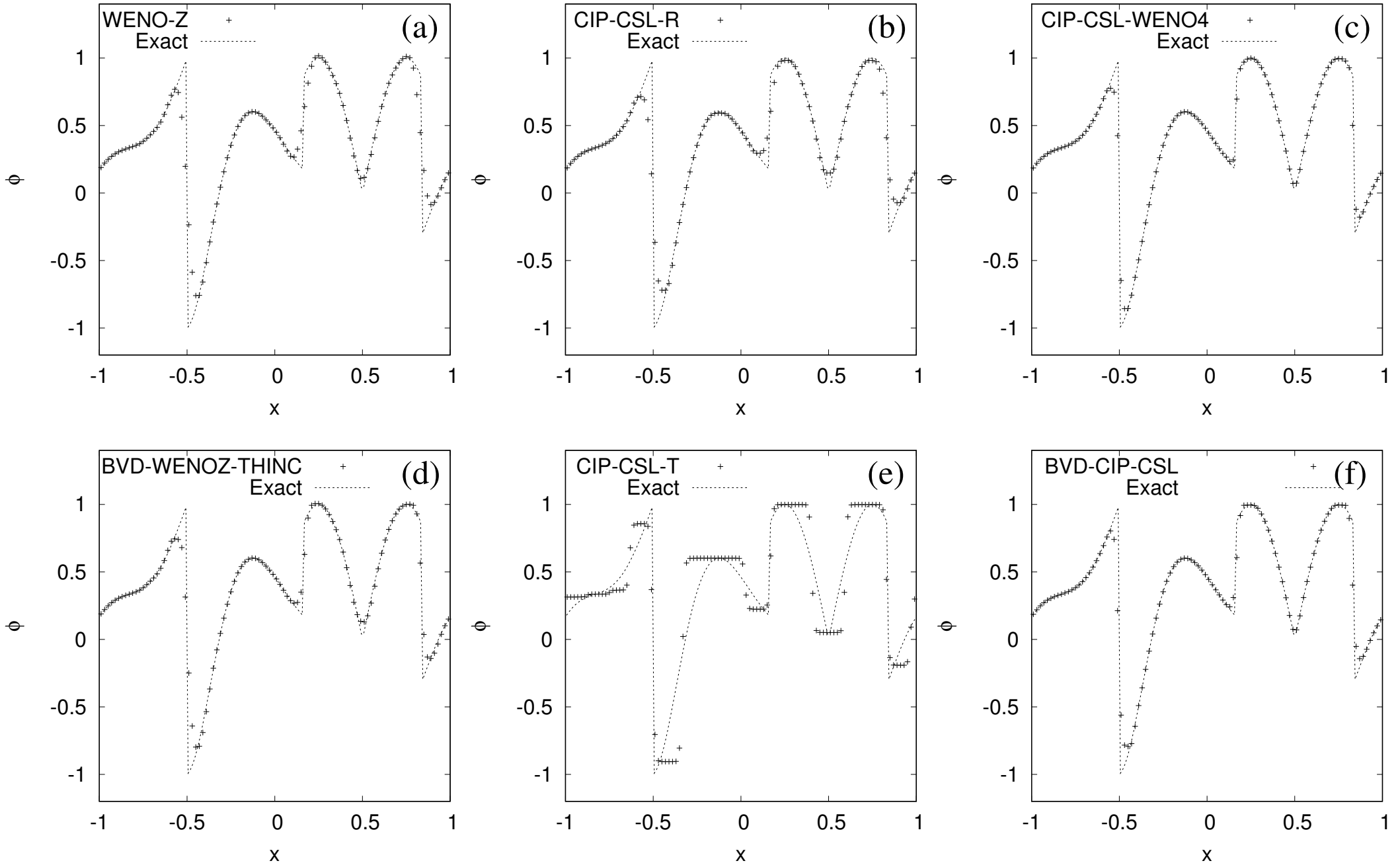
WENO-Z
Exact
(a)
CIP-CSL-R
Exact
(b)
CIP-CSL-WENO4
Exact
(c)
BVD-WENOZ-THINC
Exact
(d)
CIP-CSL-T
Exact
(e)
BVD-CIP-CSL
Exact
(f)
ϕ
x
1
0.5
0
-0.5
-1

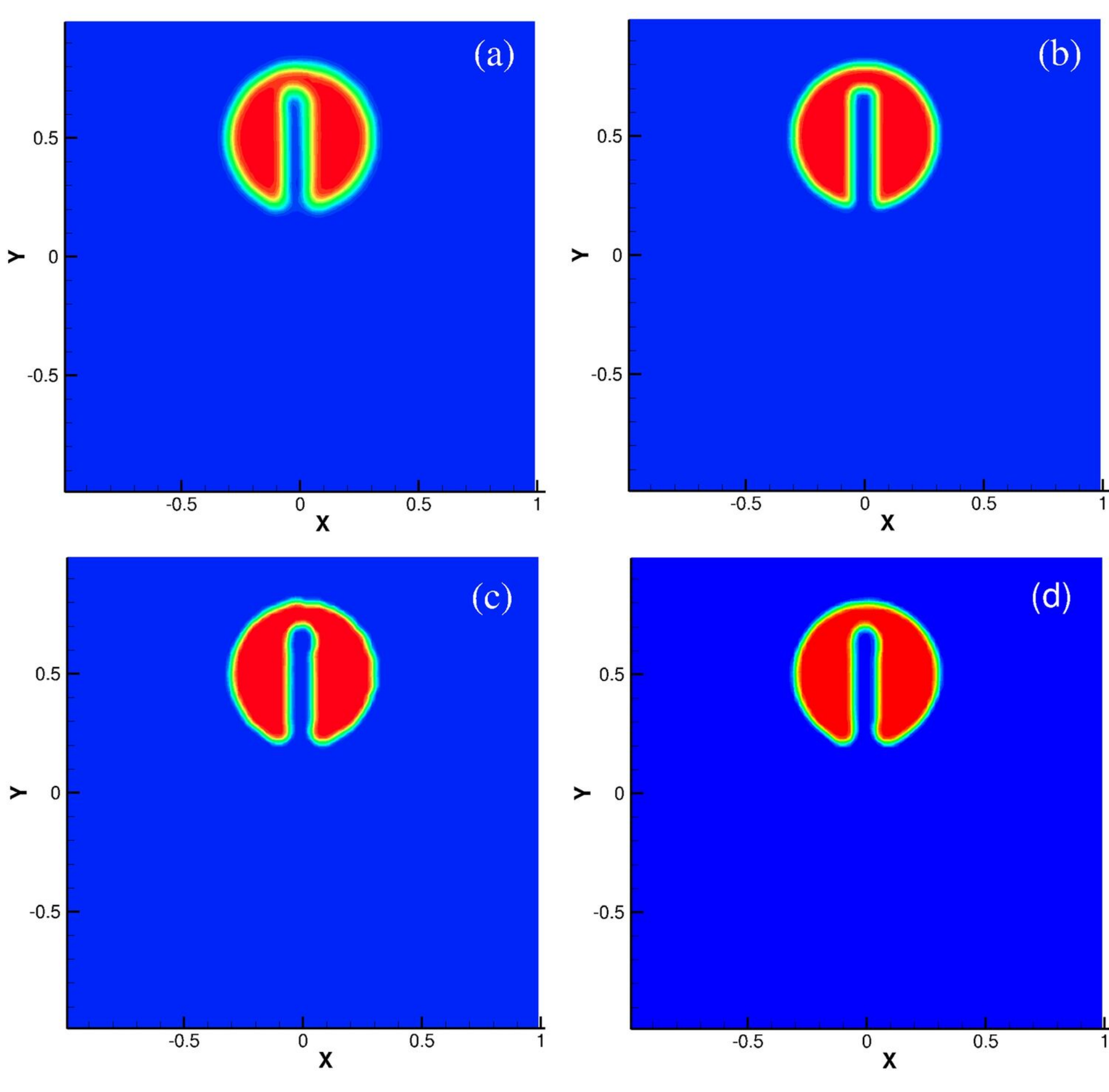
(a)
(b)
(c)
(d)
0.5
0
-0.5
Y
-0.5
0
0.5
1
X

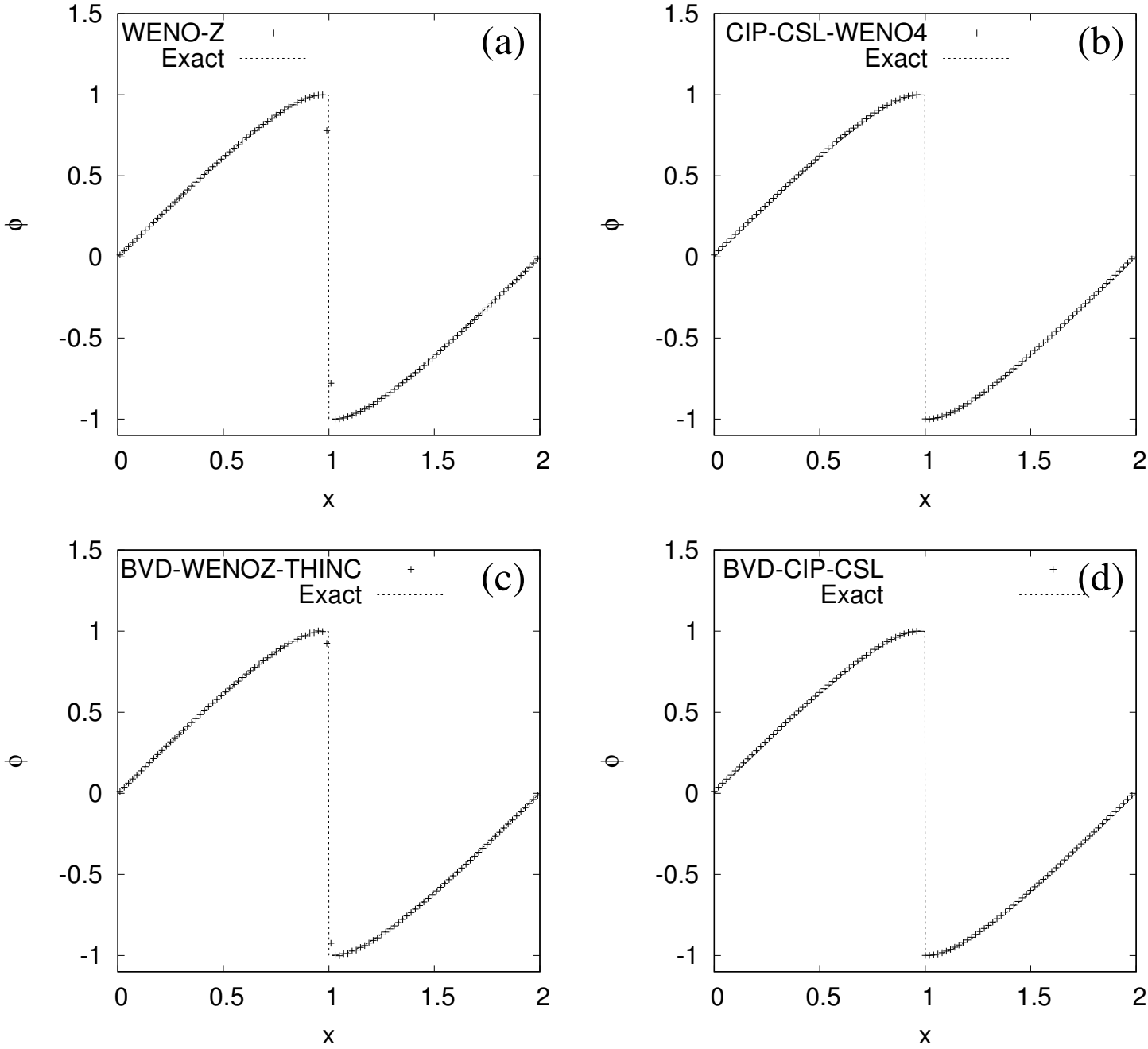
WENO-Z
Exact
(a)
CIP-CSL-WENO4
Exact
(b)
BVD-WENOZ-THINC
Exact
(c)
BVD-CIP-CSL
Exact
(d)
ϕ
x
1.5
1
0.5
0
-0.5
-1
0
0.5
1
1.5
2

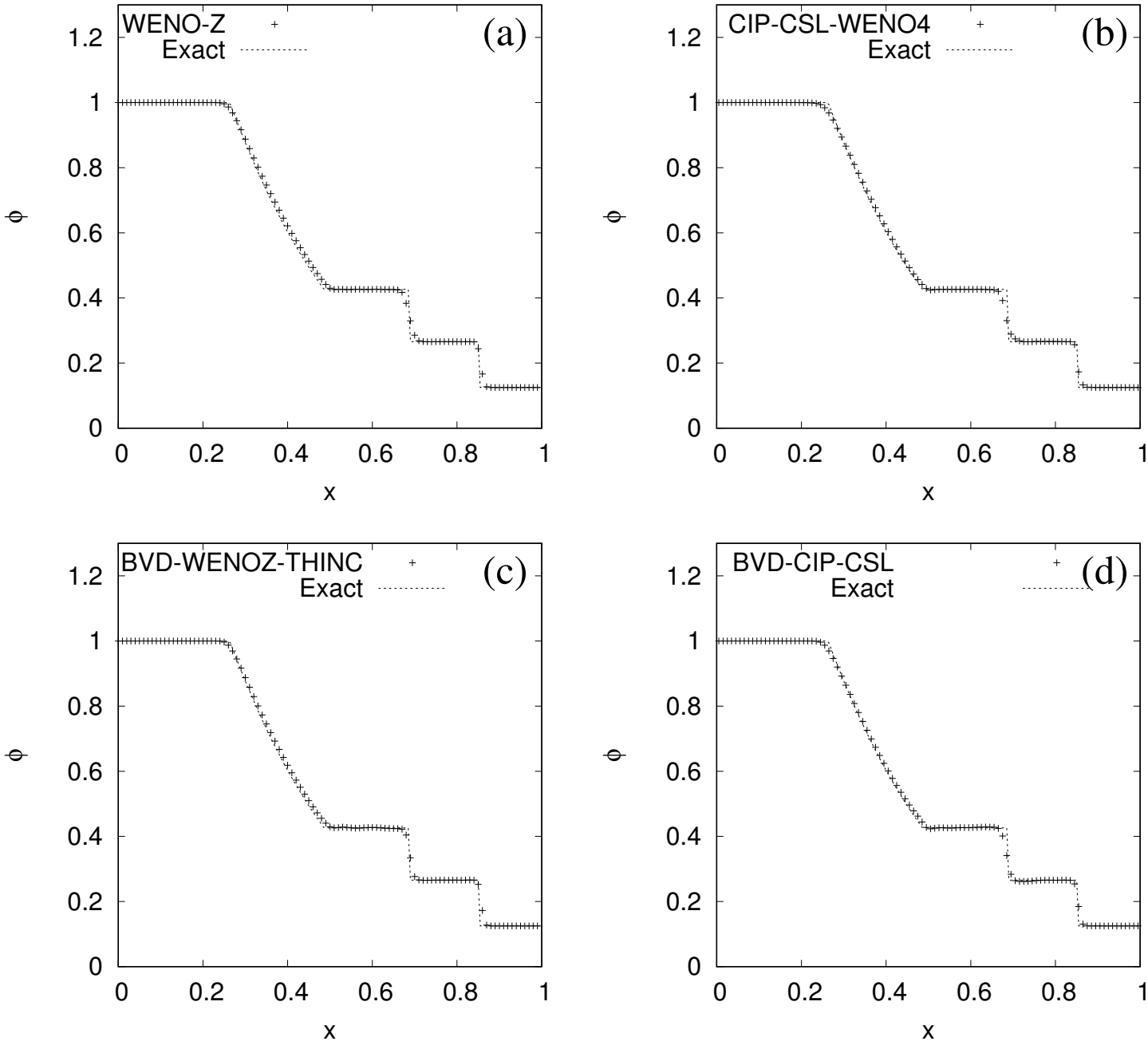
WENO-Z
Exact
(a)
CIP-CSL-WENO4
Exact
(b)
BVD-WENOZ-THINC
Exact
(c)
BVD-CIP-CSL
Exact
(d)
ϕ
x
0
0.2
0.4
0.6
0.8
1
1.2

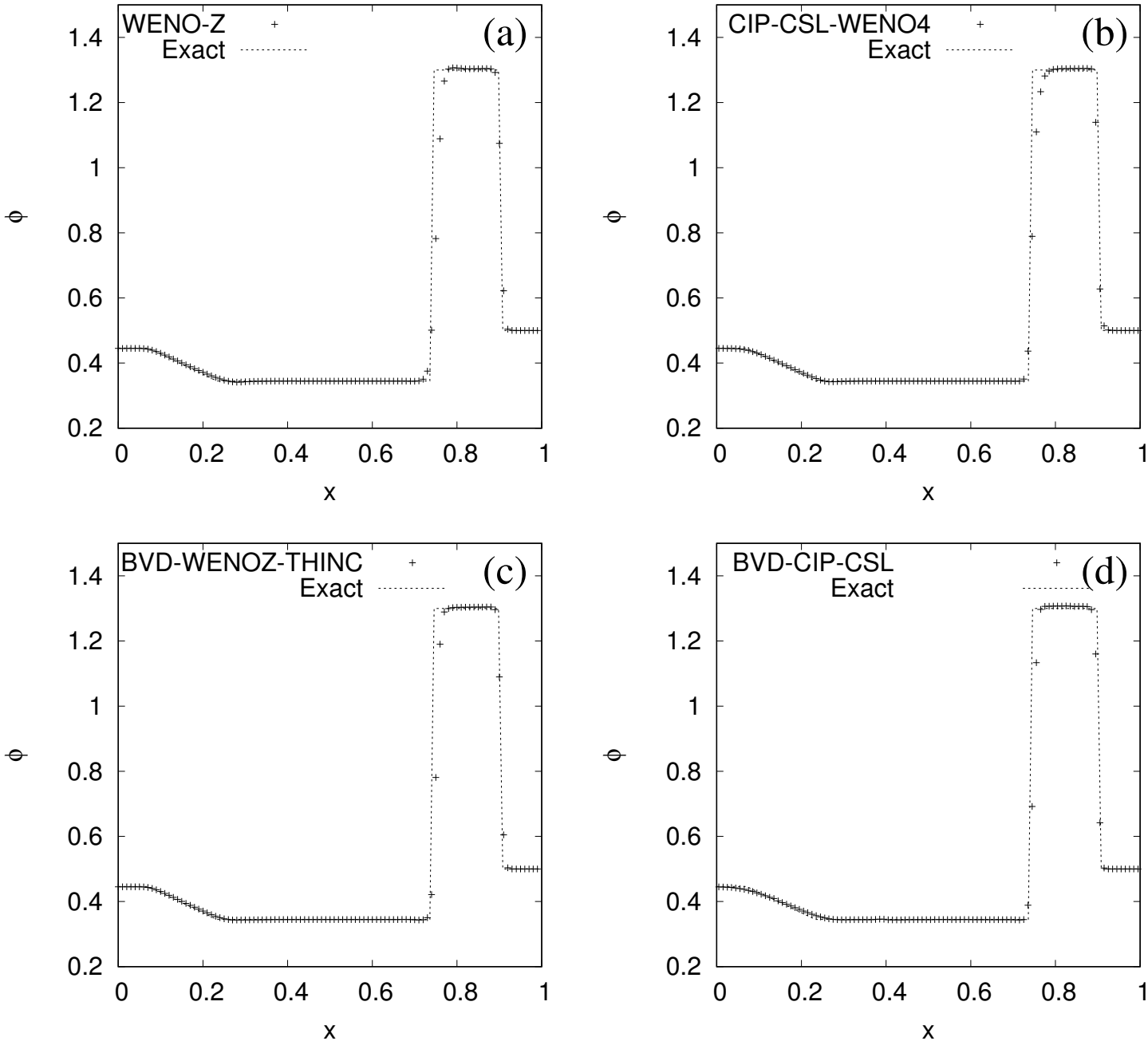
WENO-Z
Exact
(a)
CIP-CSL-WENO4
Exact
(b)
BVD-WENOZ-THINC
Exact
(c)
BVD-CIP-CSL
Exact
(d)
ϕ
x
0
0.2
0.4
0.6
0.8
1
1.2
1.4

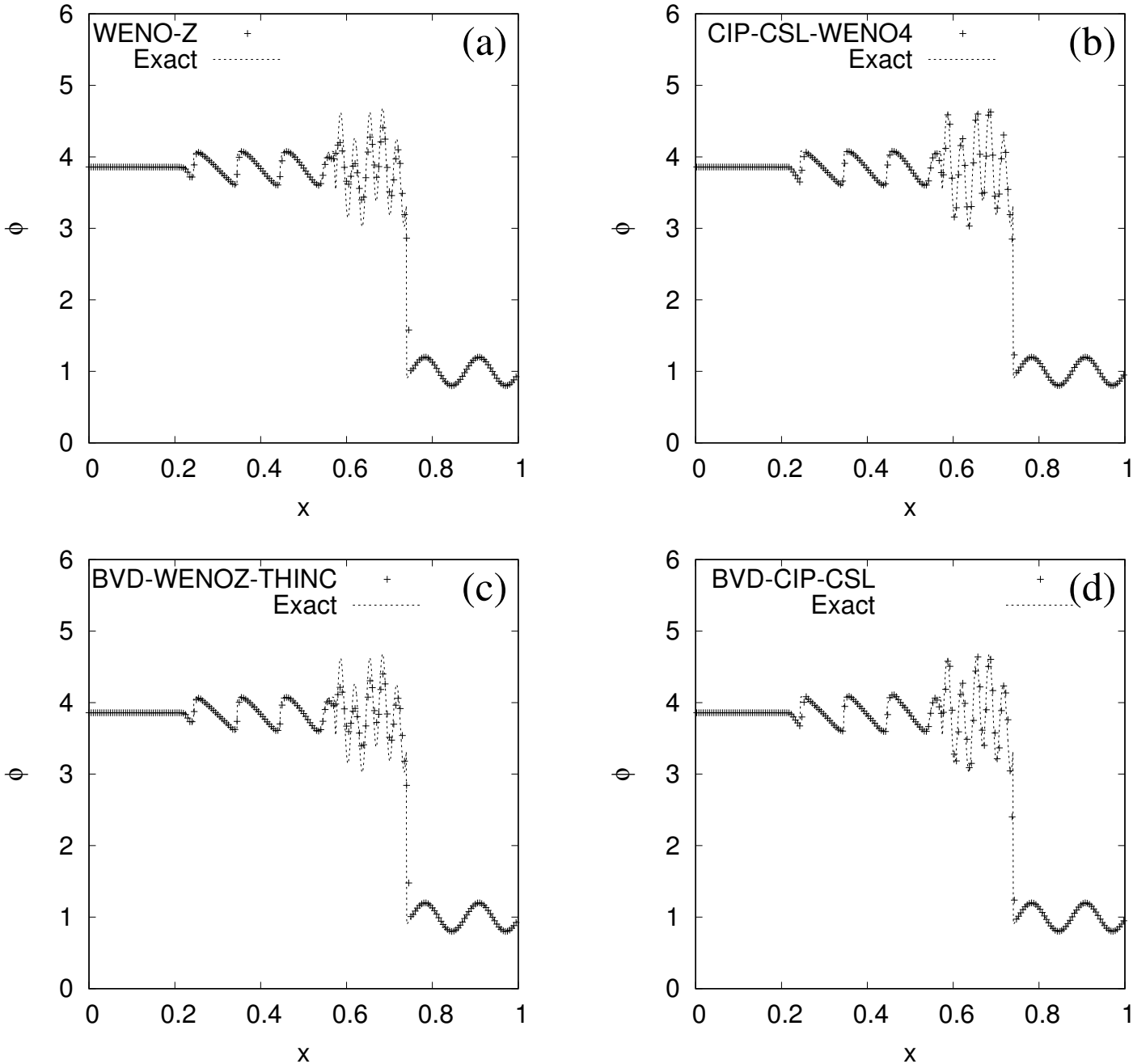
WENO-Z
Exact
(a)
CIP-CSL-WENO4
Exact
(b)
BVD-WENOZ-THINC
Exact
(c)
BVD-CIP-CSL
Exact
(d)
ϕ
x
0
1
2
3
4
5
6
0.2
0.4
0.6
0.8

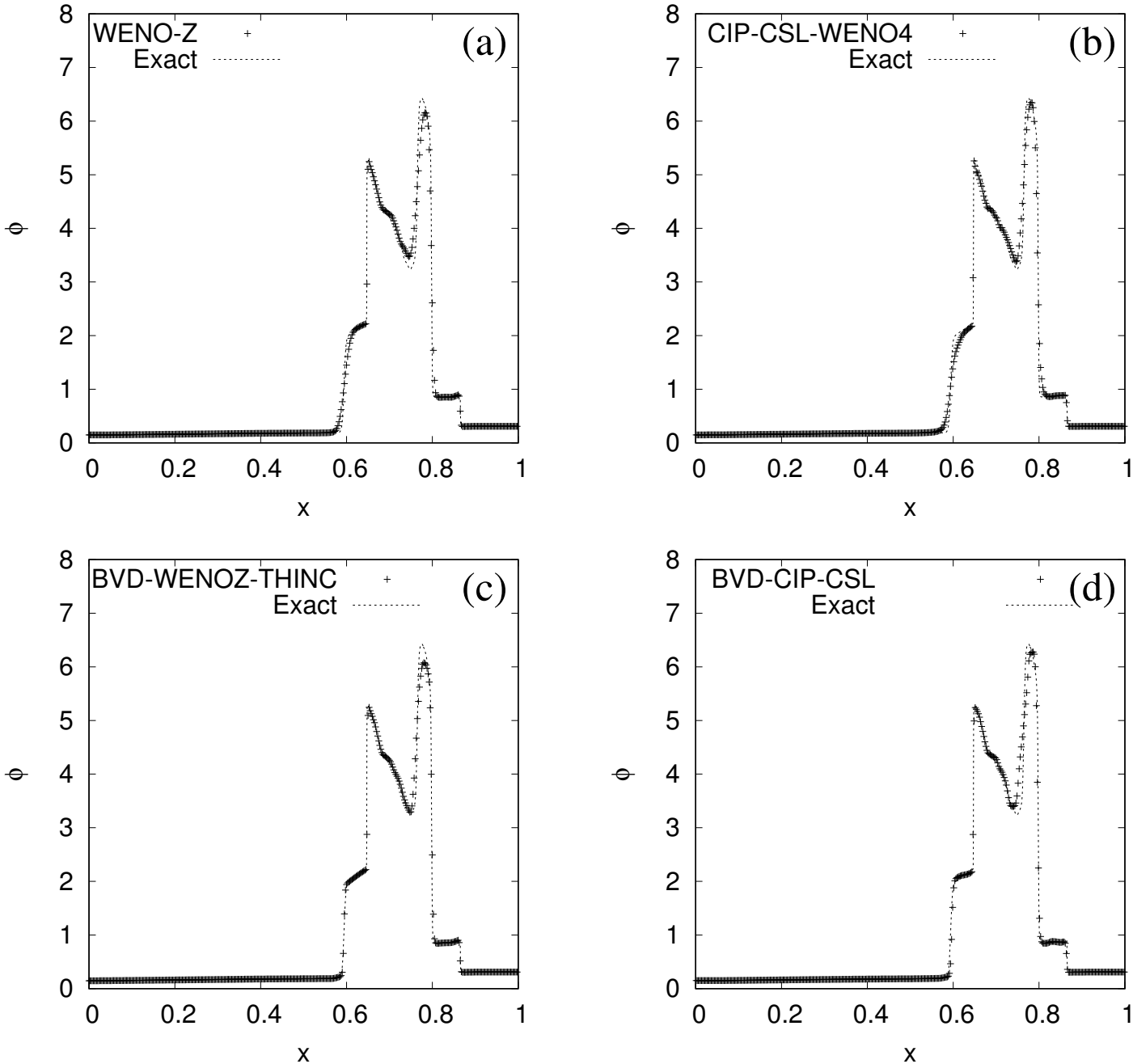
WENO-Z
Exact
(a)
CIP-CSL-WENO4
Exact
(b)
BVD-WENOZ-THINC
Exact
(c)
BVD-CIP-CSL
Exact
(d)
ϕ
x
0
1
2
3
4
5
6
7
8
0.2
0.4
0.6
0.8

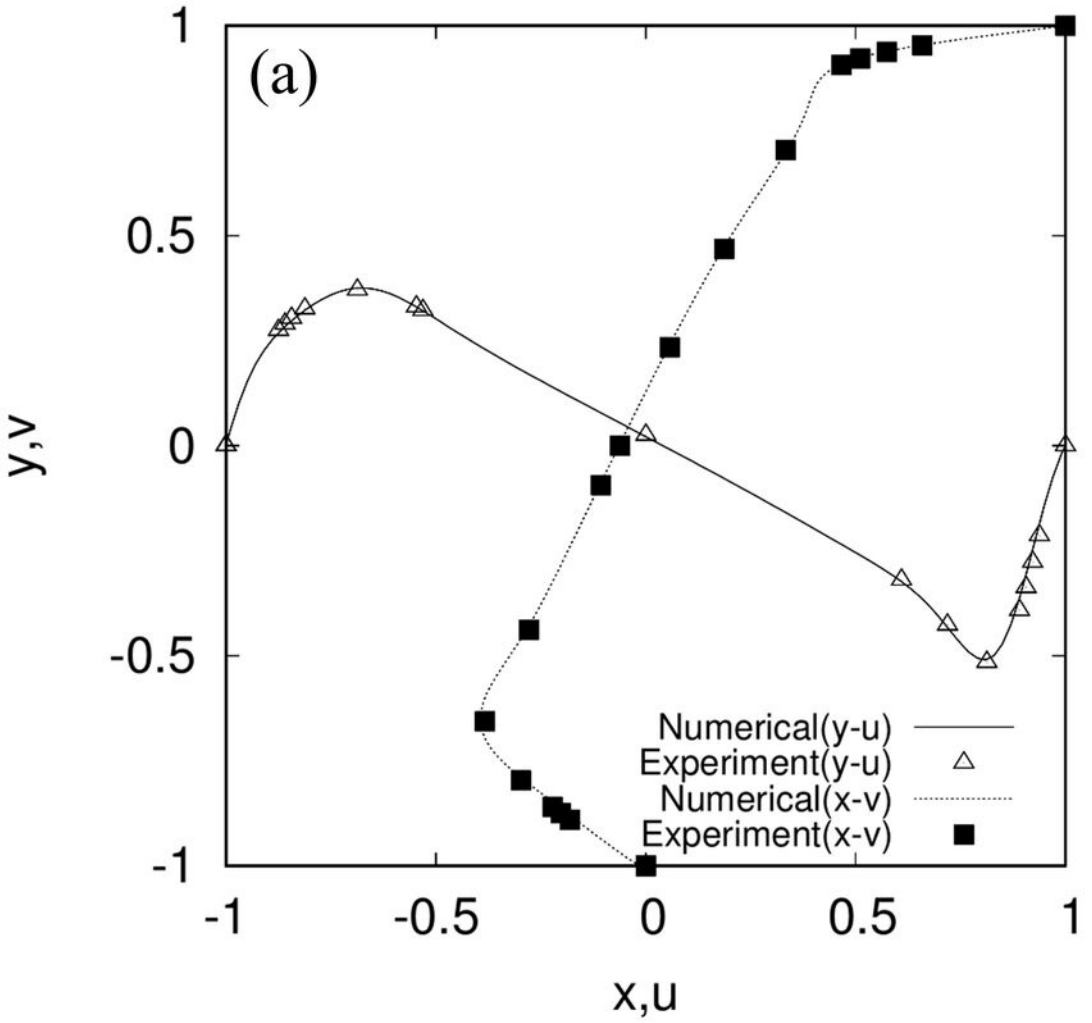
(a)
1
0.5
0
-0.5
-1
y,v
-1
-0.5
0
0.5
1
x,u
Numerical(y-u)
Experiment(y-u)
Numerical(x-v)
Experiment(x-v)

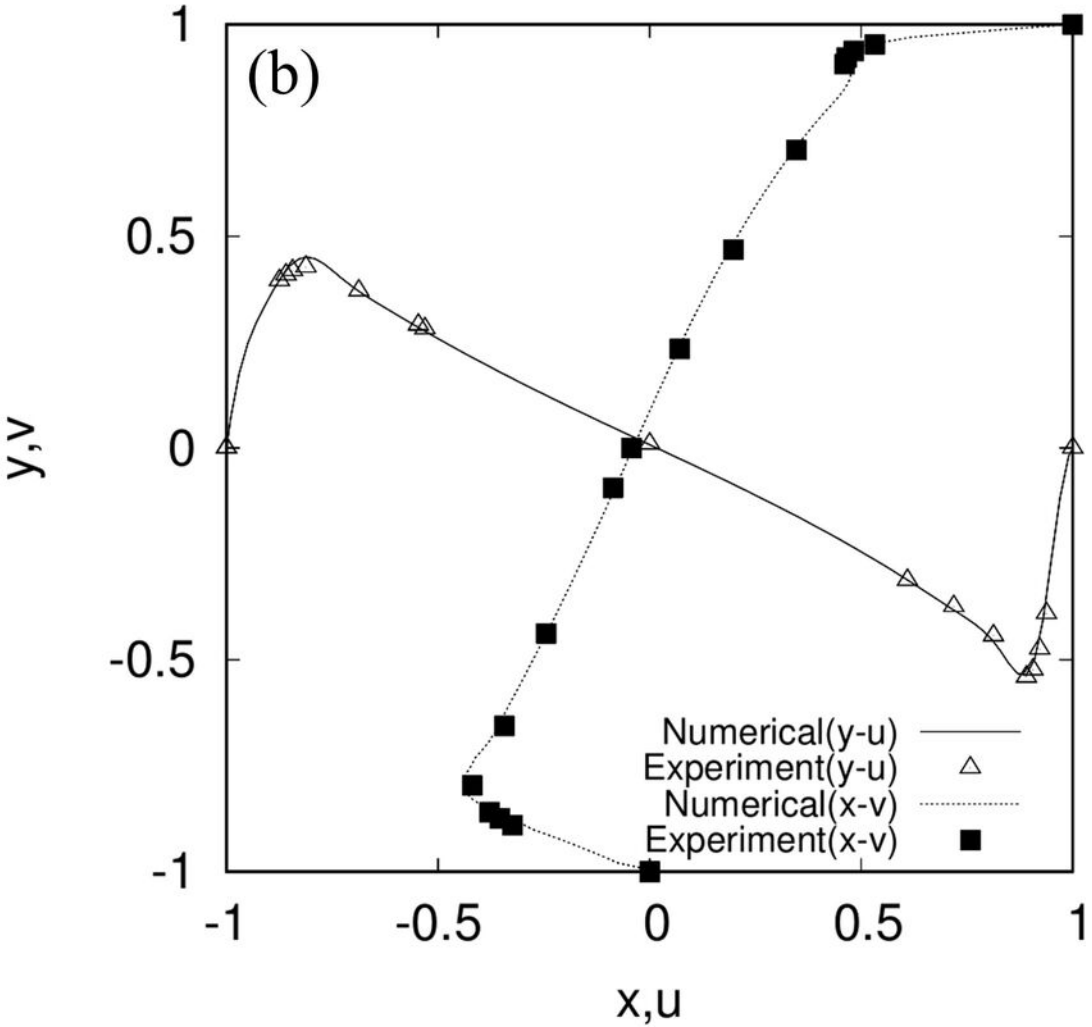
(b)
1
0.5
0
-0.5
-1
y,v
-1
-0.5
0
0.5
1
x,u
Numerical(y-u)
Experiment(y-u)
Numerical(x-v)
Experiment(x-v)

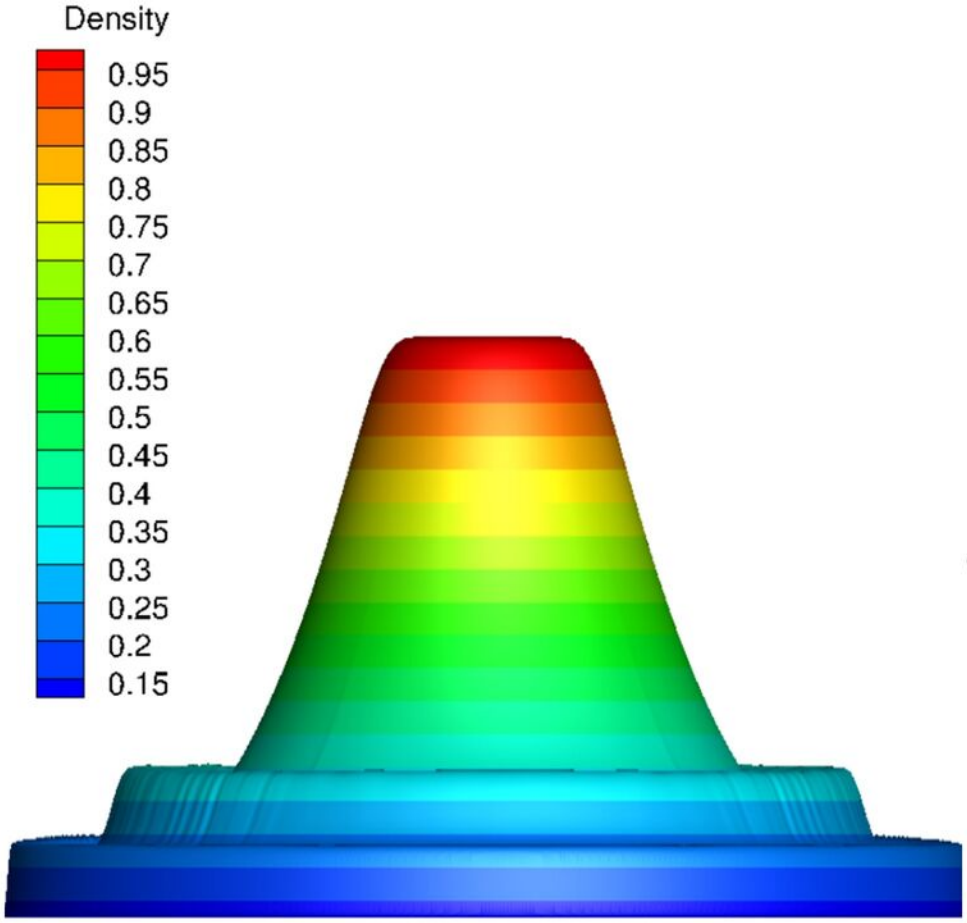
Density
0.95
0.9
0.85
0.8
0.75
0.7
0.65
0.6
0.55
0.5
0.45
0.4
0.35
0.3
0.25
0.2
0.15

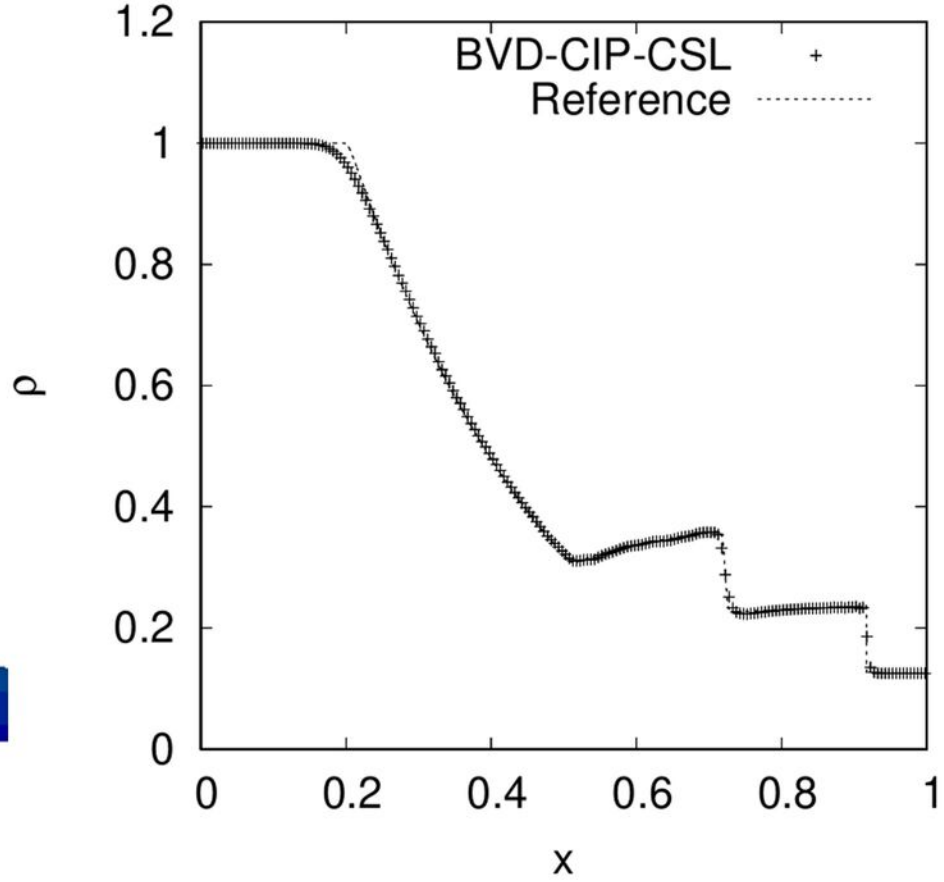
BVD-CIP-CSL
Reference
ρ
x
1.2
1
0.8
0.6
0.4
0.2
0
0
0.2
0.4
0.6
0.8
1